

MIL-101(Fe)/g-C₃N₄ for enhanced visible-light-driven photocatalysis toward simultaneous reduction of Cr(VI) and oxidation of bisphenol A in aqueous media

Zhao Feiping, Liu Yongpeng, Ben Hammouda Samia, Bhairavi Doshi, Guijarro Néstor, Min Xiaobo, Tang Chong-Jian, Sillanpää Mika, Sivula Kevin, Wang Shaobin

This is a Author's accepted manuscript (AAM) version of a publication
published by Elsevier
in Applied Catalysis B: Environmental

DOI: 10.1016/j.apcatb.2020.119033

Copyright of the original publication: © 2020 Elsevier B.V.

Please cite the publication as follows:

Zhao, F., Liu, Y., Ben Hammouda, S., Doshi, B., Guijarro, N., Min, X., Tang, C.-J., Sillanpää, M., Sivula, K., Wang, S. (2020). MIL-101(Fe)/g-C₃N₄ for enhanced visible-light-driven photocatalysis toward simultaneous reduction of Cr(VI) and oxidation of bisphenol A in aqueous media. Applied Catalysis B: Environmental, vol. 272. DOI: 10.1016/j.apcatb.2020.119033

**This is a parallel published version of an original publication.
This version can differ from the original published article.**



MIL-101(Fe)/g-C₃N₄ for enhanced visible-light-driven photocatalysis toward simultaneous reduction of Cr(VI) and oxidation of bisphenol A in aqueous media

Feiping Zhao^{a, b, c}, Yongpeng Liu^d, Samia Ben Hammouda^c, Bhairavi Doshi^c, Néstor Guijarro^d, Xiaobo Min^{a, b}, Chong-Jian Tang^{a, b, **, *}, Mika Sillanpää^e, Kevin Sivula^d, Shaobin Wang^{f, *}

^a School of Metallurgy & Environment, Central South University, Changsha, Hunan, 410083, China

^b Chinese National Engineering Research Center for Control & Treatment of Heavy Metal Pollution, Changsha, Hunan, 410083, China

^c Department of Green Chemistry, School of Engineering Science, LUT University, Sammonkatu 12, FI-50130, Mikkeli, Finland

^d Laboratory for Molecular Engineering of Optoelectronic Nanomaterials (LIMNO), École Polytechnique Fédérale de Lausanne (EPFL), Station 6, 1015, Lausanne, Switzerland

^e School of Civil Engineering and Surveying, Faculty of Health, Engineering and Sciences, University of Southern Queensland, Toowoomba, 4350 QLD, Australia

^f School of Chemical Engineering and Advanced Materials, The University of Adelaide, Adelaide, SA, 5005, Australia

ARTICLE INFO

Keywords:

Visible-light photocatalyst
Cr(VI) reduction
MIL-101(Fe)/g-C₃N₄
bisphenol-A degradation
Z-scheme heterojunction

ABSTRACT

Heterostructured composites with an excellent photocatalytic activity have attracted increasing attention because of their great application in environmental remediation. Herein, a MIL-101(Fe)/g-C₃N₄ heterojunction was synthesized via in-situ growth of MIL-101(Fe) onto g-C₃N₄ surface. The heterojunctions were applied as a bifunctional photocatalyst for simultaneous reduction of Cr(VI) and degradation of bisphenol-A (BPA) under visible light and exhibited an obvious enhancement in photocatalytic performance compared with MIL-101(Fe) or g-C₃N₄. The improved activity could be attributed to the enhanced light absorption and efficient charge carrier separation by forming a direct Z-scheme heterojunction with appropriate band alignment between MIL-101(Fe) and g-C₃N₄. The radical trapping and electron spin resonance showed that photo-generated electrons are responsible for the reduction of Cr(VI) and BPA degradation, following an oxygen-induced pathway. This work provides new insight into the construction of metal-free semiconductor/MOFs heterojunctions as a bifunctional visible-light-driven photocatalyst for efficient and simultaneous treatment of multiple toxic pollutants in water.

1. Introduction

Water contamination by heavy metals and organic pollutants has become one of the biggest environmental challenges to our world. Among heavy metals, hexavalent chromium (Cr(VI)) is a common contaminant in surface and ground water discharged from numerous industrial processes, for instance, electroplating, tanning, metallurgy, metal finishing, and petroleum refining. Researches have shown that the concentrations of Cr(VI) higher than 0.1 ppm will bring about lethal effects on aquatic life [1]. Moreover, Cr(VI) is often discharged along with hazardous organic pollutants, which makes the treatment more challenging [2,3]. Thus, it is urgent and crucial to find an efficient and sustainable approach for simultaneous treatment of the co-existed Cr(VI) and organic pollutants in wastewater. Various methods, such as adsorption, precipitation, membrane filtration, electrochemical process, and

photocatalysis have been applied for the wastewater treatment. Among them, photocatalysis has been considered as a promising approach since it realizes one-pot removal of the contaminants from water under light irradiation [4]. To date, an increasing attention has been focused on the photocatalytic reduction of Cr(VI) and oxidation of organic pollutants. However, most of these researches focused on the treatment of Cr(VI) [5] or organic pollutants [6]. Some researchers have studied the simultaneous reduction of Cr(VI) and oxidation of organic pollutants using TiO₂ [7], ZnO [8], ZrO₂ [9], Fe-doped TiO₂ [10], and ZnO-reduced graphene oxide [11]. Fu et al. reported that the presence of 4-chlorophenol could significantly enhance the photocatalytic reduction efficiency of Cr(VI) on TiO₂ [12]. However, due to the wide band gaps of these photocatalysts, their applications were limited in UV light irradiation. From a sustainable perspective, it is significant to develop efficient visible-light-driven photocatalysts for the simultaneous treatment of the co-existing pollutants in wastewater.

* Corresponding author.

** Corresponding author at: School of Metallurgy & Environment, Central South University, Changsha, Hunan, 410083, China.

Email addresses: chjtang@csu.edu.cn (C-J Tang); shaobin.wang@adelaide.edu.au (S. Wang)

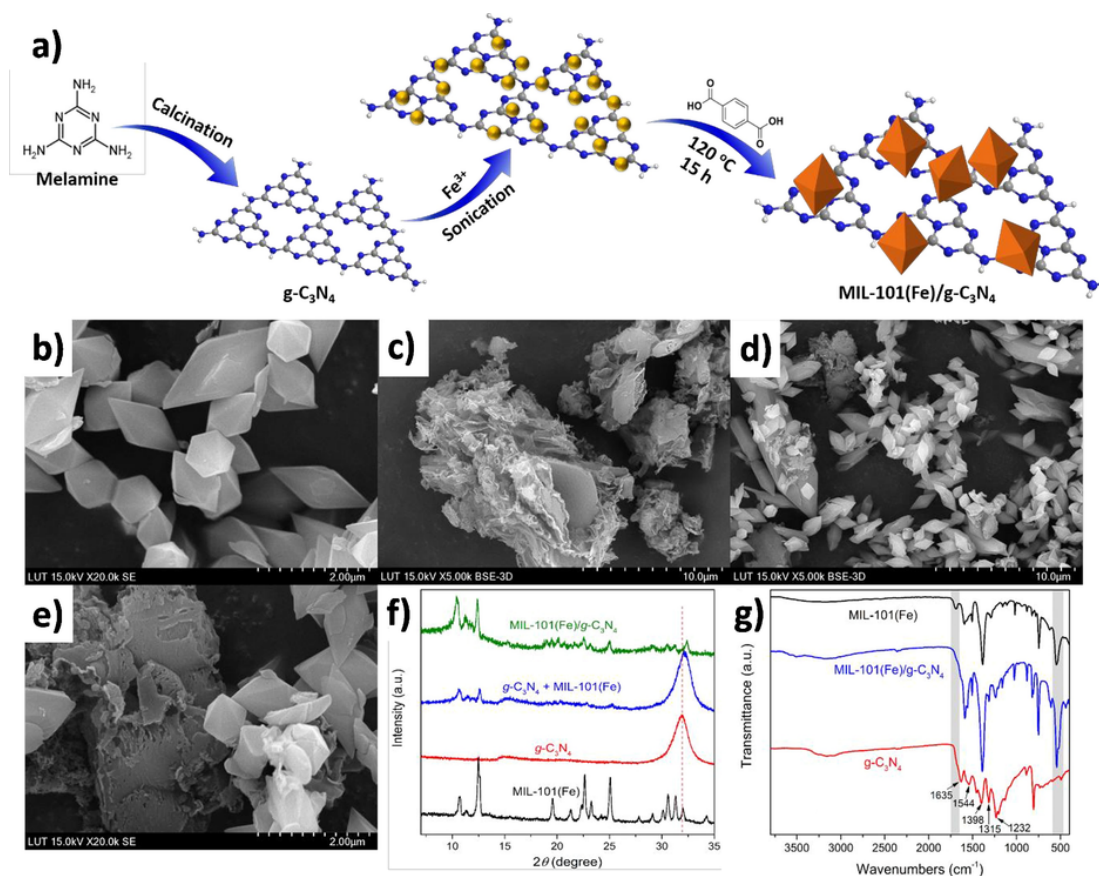


Fig. 1. Schematic diagram of MIL-101(Fe)/g-C₃N₄ synthesis (a), SEM images of MIL-101(Fe) (b), g-C₃N₄ (c), and MIL-101(Fe)/g-C₃N₄ (d and e), XRD patterns (f) and FTIR spectra (g) of the as-prepared samples.

Metal-organic frameworks (MOFs), formed by the self-assembly of metal ions with polyatomic organic bridging linkers, are a class of advanced crystalline composite and porous materials [13]. Due to their high surface area, porous structure, and tailored chemical properties, MOFs are outstanding candidates for various advanced applications such as drug delivery, gas storage, separation, purification, sensing, and heterogeneous catalysis since their synthesis [14]. Owing to the synergistic effect arising from the catalytically reactive sites (transition metal centers and organic linkers) of MOFs, some of them can harvest light and undergo a photochemical process after photo-excitation [15]. This implies that they are potentially versatile and tunable photocatalysts [16]. For example, MOF-5 has been successfully applied as a photocatalyst for phenol removal under UV light irradiation [17]. Wu's group has reported that Zr- and In-based MOFs performed a considerable photocatalytic activity in Cr(VI) reduction [18,19]. More recently, a series of Fe(III)-based MOFs, such as MIL-53(Fe), MIL-68(Fe), MIL-88(Fe), MIL-100(Fe), and MIL-101(Fe), have been reported to be applied for the decolorization of dyes or reduction of Cr(VI) under visible light irradiation [20–24]. Despite the fact that MOF photocatalysts have made considerable headway in the past decades, their photocatalytic performance is still not good enough due to their low efficiency for solar energy conversion, low conductivity, and rapid e⁻/h⁺ recombination [25]. In this regard, many efforts have been made to remedy these drawbacks through constructing heterostructures with a noble metal or metal oxide such as Pd, Ag, Pt, and Au [24][26]. This strategy can tune the photocatalytic performance of many MOFs, but the high cost of the noble metals, complicated fabrication procedures, and photochemical instability limit their practical application. Therefore, it is valuable to find low-cost and highly synergistic complementary materi-

als and facile approaches to fabricate MOF-based heterojunction photocatalysts.

Graphitic carbon nitride (g-C₃N₄), a novel metal-free semiconductor with an unique graphene-like 2D structure, has recently aroused numerous interest in water splitting [27], CO₂ reduction [28], and pollutant degradation [29]. Researchers are convinced of the extraordinary advantages of g-C₃N₄ as a visible-light responsive photocatalyst: its raw material abundance, facile fabrication methods, chemical stability, high solar light absorption, and a suitable band gap (ca. 2.7 eV) [30]. However, the performance of bulk g-C₃N₄ is still far from satisfactory for practical application, due to its low specific surface area and high recombination rate of photo-generated electron-hole pairs. An efficient strategy is to couple g-C₃N₄ with other semiconductors to form heterostructured composites so that the photo-generated charges can be separated rapidly, subsequently enhancing their photocatalytic activity [31]. Moreover, as mentioned above, an important asset of MOFs is their high surface area and porous structure, which was found as very advantageous in the formation of their composites with g-C₃N₄ [25]. These MOF/g-C₃N₄ hybrid composites were presented as excellent catalysts due to the improved pore volume, decreased recombination rate of the photo-generated charges, and wider spectrum absorption of sunlight. Moreover, similar to graphene, bulk g-C₃N₄ suffers from the inevitable restacking when it is used alone [32]. MOFs can act as the spacer between g-C₃N₄, which prevents g-C₃N₄ from restacking and aggregation [25]. The g-C₃N₄ has been coupled with various semiconductor materials to form heterojunctions, such as TiO₂/g-C₃N₄ [32], g-C₃N₄/MoS₂ [33], g-C₃N₄/BiPO₄ [34], Bi₁₂GeO₂₀/g-C₃N₄ [35], and perovskite oxide/g-C₃N₄ [36]. However, the aforementioned MOF/g-C₃N₄ heterojunctions have less been studied. Giannakoudakis et al. have synthesized unique composites of copper-based MOF (Cu-BTC) with g-

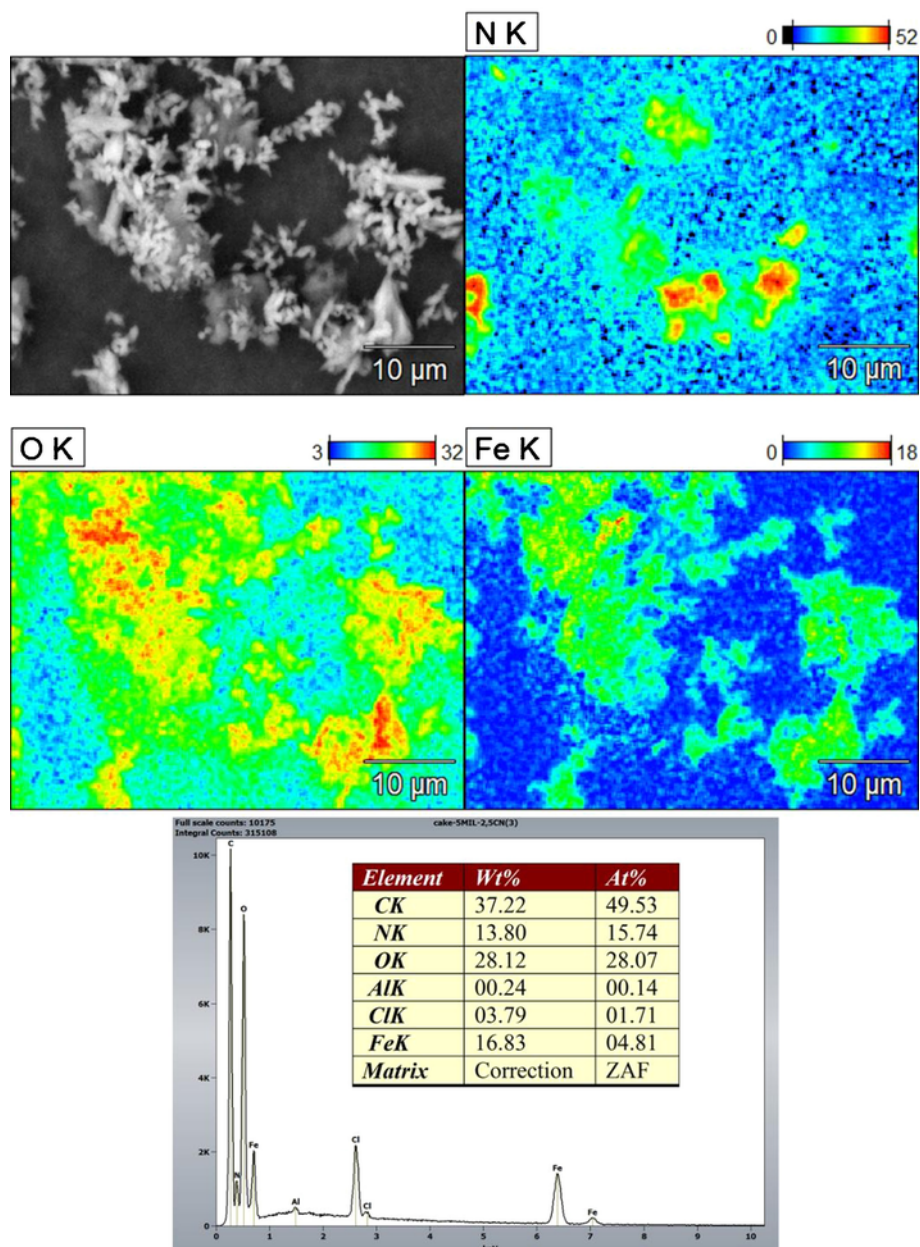


Fig. 2. EDS elemental mapping of MIL-101(Fe)/g-C₃N₄ (O, Fe from MIL-101(Fe) and N from g-C₃N₄) and EDS spectra of MIL-101(Fe)/g-C₃N₄ (inset Table shows the elemental compositions).

C₃N₄, which showed the enhanced photocatalytic performance under visible light [25]. Ni-Zn-MOF/g-C₃N₄ nanoparticles were prepared via an in situ synthesis method for the detection of volatile polycyclic aromatic hydrocarbons [37]. Xu et al. anchored co-catalysts onto UiO-66-NH₂/g-C₃N₄ hybrids, revealing an effective way to obtain heterostructured photocatalysts for H₂ production from water splitting [38]. To the best of our knowledge, however, there is no report about the MOF/g-C₃N₄ for the simultaneous photocatalytic reduction of Cr(VI) and oxidation of organic pollutants.

In this work, we developed a hybrid of g-C₃N₄ and iron-based metal-organic framework (MIL-101(Fe)/g-C₃N₄) heterojunctions in a facile in-situ synthesis approach for the simultaneous treatment of Cr(VI) and bisphenol A (BPA). MIL-101(Fe), which has a zeotype crystal structure consisting of two kinds of cages with internal diameters of 29 and 30 Å [39], was chosen in this work owing to its stability, non-toxic nature, extremely large surface area, numerous active transition

metal sites, and visible light response [40]. In this set, the MIL-101(Fe) was applied as the support skeleton, which plays a vital role in the formation of the architectures with high surface area and rich metal sites, and preventing g-C₃N₄ from restacking. Meanwhile, the incorporated g-C₃N₄ can help harness a wider spectrum of solar light [29]. The integration of MIL-101(Fe) and g-C₃N₄ is expected to promote advantages of each component and to overcome mutual disadvantages by enhancing the transfer rate of the photo-generated electron-hole pairs. Bisphenol A (BPA), which is a widely used starting material for the synthesis of plastics with the world production capacity of 3.6 million tonnes yearly, has been listed as a hazardous endocrine disruptor by the European Chemicals Agency since 2017 [41]. In our previous works, we have reported the sulfate radical-mediated degradation of Bisphenols by perovskite materials [42–44]. Herein we firstly report to use bisphenol A as a hole scavenger in the photocatalytic Cr(VI) reduction system, as most of previous works use ammonium formate, ammonium

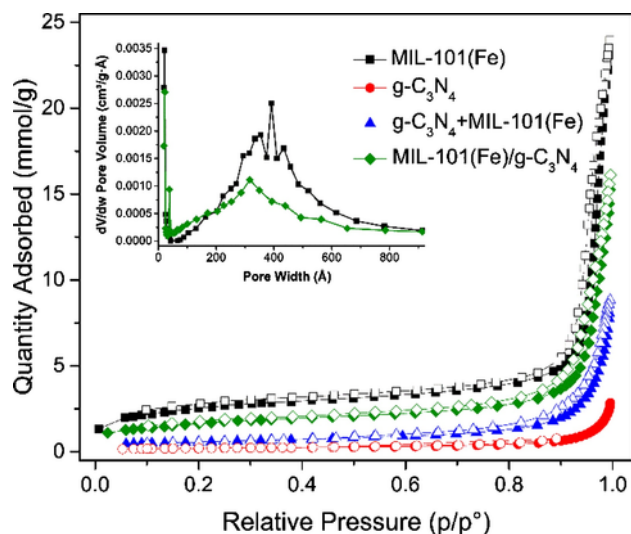


Fig. 3. N_2 adsorption/desorption isotherms of MIL-101(Fe), $g-C_3N_4$, $g-C_3N_4 + MIL-101(Fe)$, and MIL-101(Fe)/ $g-C_3N_4$. Inset: pore size distributions of MIL-101(Fe) and MIL-101(Fe)/ $g-C_3N_4$.

Table 1

The BET specific surface (S_{BET}), pore volume (V_p) and pore size (D) of MIL-101(Fe), $g-C_3N_4$, $g-C_3N_4 + MIL-101(Fe)$, and MIL-101(Fe)/ $g-C_3N_4$.

Samples	S_{BET} (m^2/g)	V_p (cm^3/g)	D (nm) ^a
MIL-101(Fe)	198.7	0.78	25.1/28.3
$g-C_3N_4$	15.4	0.09	27.0/25.7
$g-C_3N_4 + MIL-101(Fe)$	44.0	0.27	28.9/25.3
MIL-101(Fe)/ $g-C_3N_4$	131.6	0.51	21.3/24.2

^a The pore diameters were calculated from the adsorption/desorption branch of the isotherm using the BJH method.

oxalate [19], or dyes [45] as hole scavengers. The photocatalytic mechanisms induced by visible light responsive MIL-101(Fe)/ $g-C_3N_4$ were also proposed to demonstrate the simultaneous reduction of Cr(VI) and oxidation of bisphenol A.

2. Experimental

2.1. Materials

All the chemicals used in this study were purchased from Sigma-Aldrich (Finland). All the chemicals were of analytical grade and were used as received without further purification.

2.2. Synthesis of $g-C_3N_4$, MIL-101(Fe), and MIL-101(Fe)/ $g-C_3N_4$

$g-C_3N_4$ powder was synthesized according to the methods reported previously [25,46]. Briefly, 5 g of melamine was added into a crucible covered loosely by a lid and heated in a muffle furnace at 550 °C for 4 h (heating rate of 5 °C /min). After cooling to room temperature, the obtained yellow bulk $g-C_3N_4$ was grinded into powder in a mortar and re-calcined in an open crucible without a lid at 530 °C for 3 h (heating rate of 10 °C /min), to make sure the raw melamine can be converted to $g-C_3N_4$ completely. MIL-101(Fe) was prepared by a solvothermal method [39] with some modifications. Typically, a mixture of 1.76 g (6.50 mmol) of $FeCl_3 \cdot 6H_2O$, 0.54 mg of 1,4-benzenedicarboxylic acid (H_2BDC , 3.25 mmol), and 80 mL of dimethylformamide (DMF) was sonicated and then heated at 120 °C for 15 h in a Teflon-lined stainless steel autoclave. After cooling naturally to room temperature, the resulted orange solid was collected by centrifugation at 3000 rpm and then stirred in 200 mL of methanol for 3 days (methanol changed once

per day) to remove the guest molecules in the pores of the MOF material. The purified sample was separated by centrifugation and dried under vacuum at 100 °C for 20 h.

MIL-101(Fe)/ $g-C_3N_4$ heterojunction was prepared by dispersing 92 mg $g-C_3N_4$ powder (1.0 mmol) in the well-dissolved ferric chloride/DMF solution under 30 min stirring to reach equilibrium, and then H_2BDC was added with 30 min of sonication. After a solvothermal treatment, the resulting solid was subsequently washed by methanol and subjected to the similar synthesis procedure to that of MIL-101(Fe). The schematic diagram of MIL-101(Fe)/ $g-C_3N_4$ synthesis is presented in Fig. 1a.

2.3. Characterizations

X-ray diffraction (XRD) patterns were recorded on a PANalytical Empyrean diffractometer with a Co-K X-ray irradiation source ($\lambda = 0.17809$ nm) operated at 40 kV and 40 mA. Raman spectra were acquired on a Renishaw inVia Reflex Raman Microprobe with a laser excitation wavelength of 530 nm. Fourier transform infrared spectra (FTIR) were conducted on a Bruker Vertex 70 model with a platinum ATR accessory. The Brunauer-Emmett-Teller (BET) surface area and pore structure were measured with a Tristar®II Plus by nitrogen adsorption isotherms in the range of relative pressure from 0.0 to 1.0. Scanning electron microscopy (SEM) was performed on a Jeol JSM-5800 instrument. Elemental mapping was simultaneously performed during the SEM examination by Thermo Scientific Ultra Dry SDD Energy-dispersive X-ray spectroscopy (EDS). X-ray photoelectron spectra (XPS) were recorded on a Thermo Fisher Scientific ESCALAB 250Xi with a monochromatic Al K α X-ray source (1486.6 eV) and an X-ray beam of around 900 μ m. UV-vis diffuse reflectance spectra (UV-vis DRS) were obtained by a UV-vis spectrophotometer (Agilent Cary 60) and the data were converted to Kubelka-Munk functions. The photoluminescence spectra (PL) were determined by a fluorescence spectrometer (Hitachi F-7000). Electrochemical impedance spectroscopy (EIS) and Mott-Schottky analysis were performed using a Bio-Logic SP-300 potentiostat with a 3-electrode configuration including photocatalyst working electrode, Ag/AgCl reference electrode and Pt counter electrode in a Cappuccino-type electrochemical cell. Thermogravimetric analysis (TGA) was performed using a NETZSCH TG 209F1 (Germany) at a heating rate of 10 °C/min under a nitrogen atmosphere from 30 to 1000 °C.

2.4. Photocatalytic activity

The photocatalytic reduction of aqueous Cr(VI) to Cr(III) was carried out at 30 °C in a 80 mL quartz vial containing 20 mg of photocatalyst and 40 mL of 20 mg/L Cr(VI) aqueous solution. The effect of pH on the photocatalysis was studied in a pH range of 3-6. The pH of solutions were adjusted with 2 M H_2SO_4 . Nitrogen was purged and then 5 mg of $(NH_4)_2C_2O_4$ (hole scavenger) was added into the solution, followed by stirring in dark for 30 min to reach sorption equilibrium. The suspensions were irradiated by a 150 W halogen cold light source (Visi-Light® CL150, EU-pistoke) with a 420 nm cut-off filter. During the illumination process, 2 mL solution was collected at a certain time interval and then centrifuged at 7500 rpm for 5 min to remove the suspended catalyst. The Cr(VI) reduction was determined colorimetrically at 540 nm using the diphenylcarbazide (DPC) method with a detection limit of 5 μ g/L [47] by a PerkinElmer Lambda 365 UV-vis spectrophotometer. A pseudo-first-order kinetics was fitted for the estimation of reaction rate constants.

The simultaneous photocatalytic reduction of Cr(VI) and degradation of bisphenol A (BPA) was conducted in a system of 20 mg/L Cr(VI) with 20 mg/L BPA at natural pH (ca. 6.8) without adding any other hole scavengers. The BPA concentration was measured by a Shimadzu

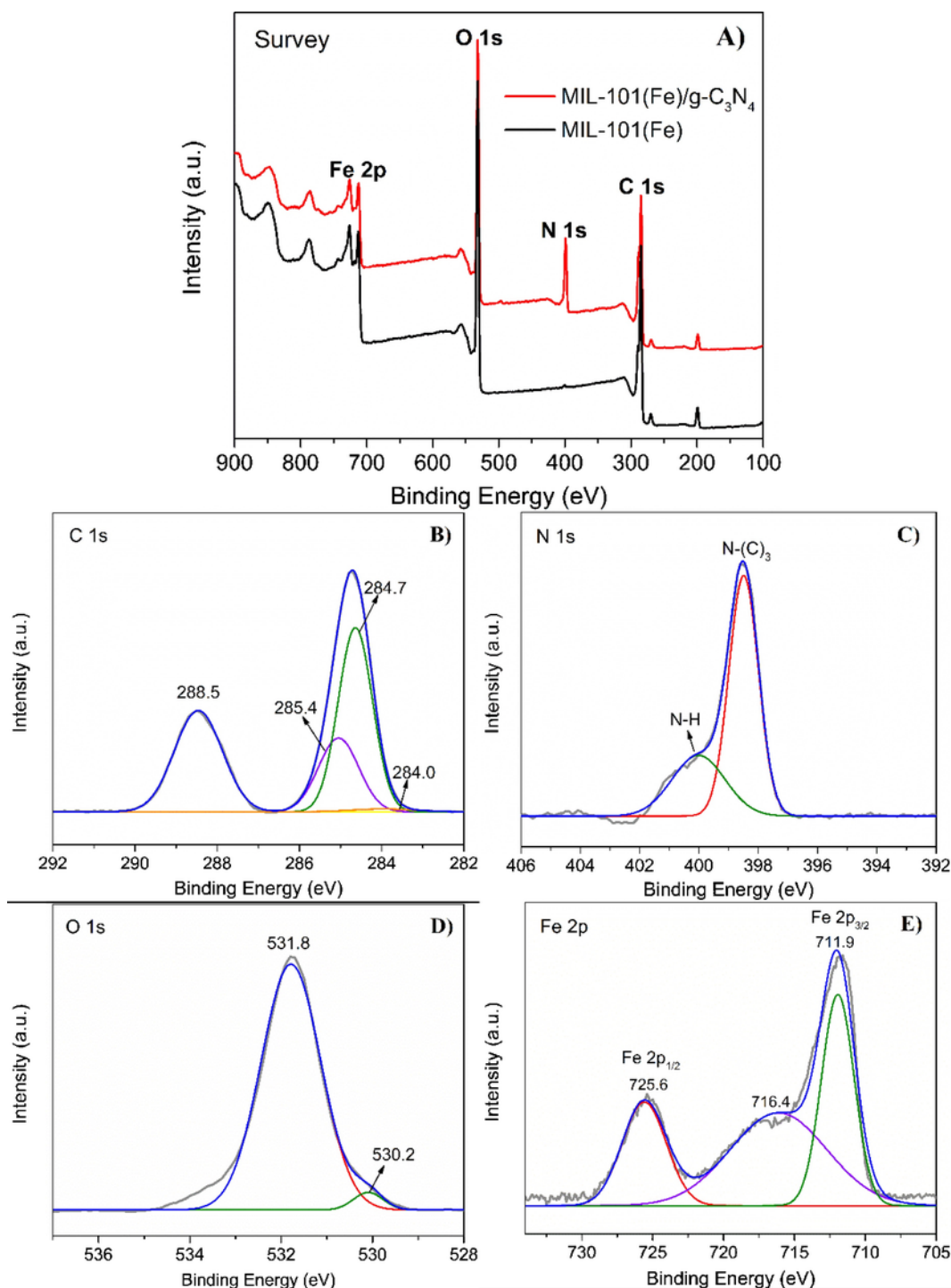


Fig. 4. The XPS survey spectra of MIL-101(Fe) and MIL-101(Fe)/g-C₃N₄ (a), C 1s (b), N 1s (c), O 1s (d), and Fe 2p (e) spectra of MIL-101(Fe)/g-C₃N₄ heterojunction.

High Performance Liquid Chromatograph equipped with a UV detector (HPLC-UV) and a Kinetex column C18 (5 m, 4.6 × 150 mm). The wavelength of the UV detector was set at 269 nm. The mobile phase was composed of 20 mM (phosphoric acid) potassium buffer solution (pH 2.5) and acetonitrile, with an isocratic percentage composition of 50:50 and flow rate of 1.0 mL/min.

2.5. Radical species trapping and electron spin resonance (ESR) experiments

In the experiments of trapping radical species, 2 mM of 1,4-benzoquinone (BQ), 2 mM of isopropanol (IPA), and 2 mM of Na₂C₂O₄ were used as scavengers for O₂^{•-}, •OH and h⁺, respectively, in the photocatalytic process. ESR spectra were recorded using a CMS-8400 paramagnetic resonance spectrometer under the following conditions: magnetic

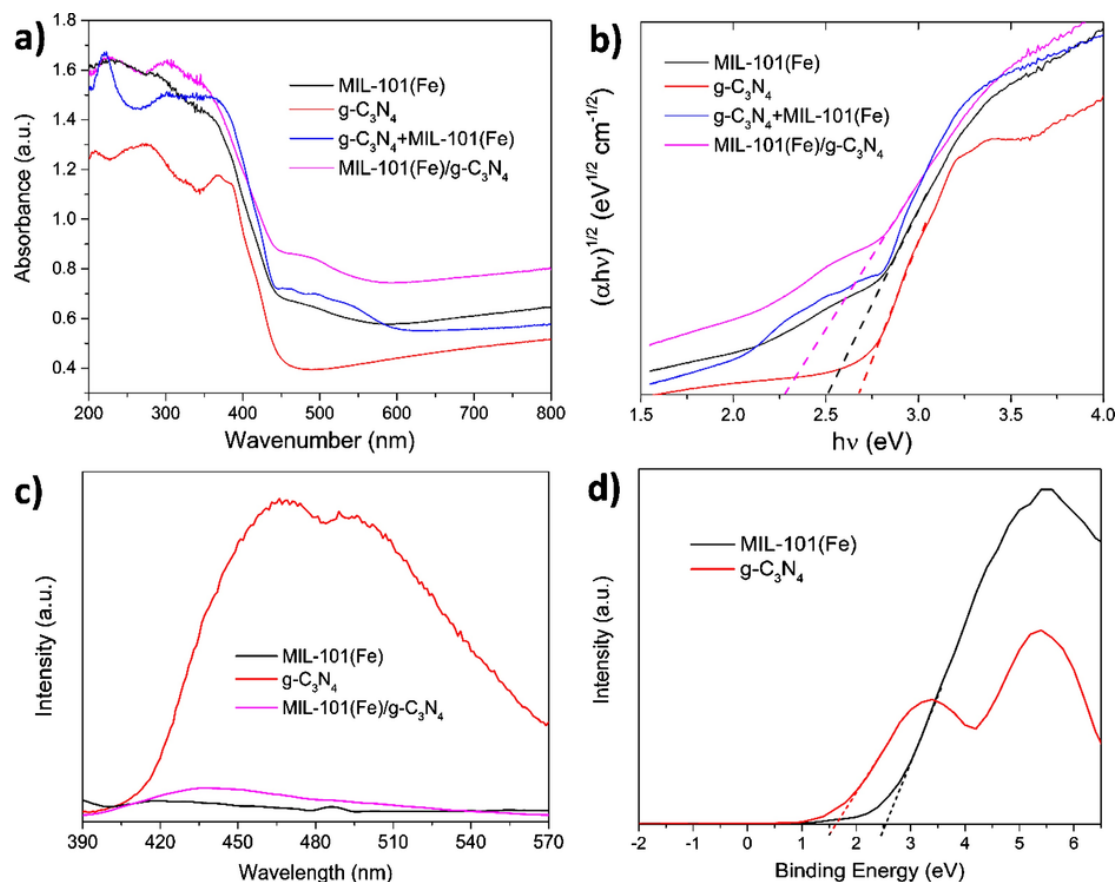


Fig. 5. DRS of MIL-101(Fe), g-C₃N₄, g-C₃N₄ + MIL-101(Fe), and MIL-101(Fe)/g-C₃N₄ (a), the plots of transformed Kubelka-Munk function vs. the light energy of the samples (b), the PL spectra of MIL-101(Fe), g-C₃N₄ and MIL-101(Fe)/g-C₃N₄ (c) and VB-XPS spectra of MIL-101(Fe) and g-C₃N₄ (d).

field 336.5 ± 6.0 mT width, power attenuation 10 dB, field modulation 0.100 mT, sweep time 100 s, microwave frequency 9450 MHz.

3. Results and discussion

3.1. Characterizations

SEM images of MIL-101(Fe), g-C₃N₄, and MIL-101(Fe)/g-C₃N₄ are shown in Fig. 1b–e. It is clearly shown that MIL-101(Fe) consists of a uniform octahedral structure with an average edge length of μm -scale (Fig. 1b), which is in good agreement with the previously reported MIL-101(Fe) [48]. g-C₃N₄ shows a two-dimensional (2D) structure with rugged surface (Fig. 1c). For the MIL-101(Fe)/g-C₃N₄ composite, it can be seen that the g-C₃N₄ and MIL-101(Fe) components were bonded together with a good contact (Fig. 1d and e). Moreover, it is also observed that the sizes of the MIL-101(Fe) crystals in the MIL-101(Fe)/g-C₃N₄ composites were significantly smaller than those of the pristine ones, indicating that the introduction of g-C₃N₄ in the precursors had some influences on the formation of the MOF crystals during the synthesis [49]. TEM was commonly employed to characterize the morphology and estimate the particle size [50]. As shown in Fig. S1a and b, the TEM images reveal that the MIL-101(Fe) crystal was closely anchored on the surface of two-dimensional g-C₃N₄ sheets. The length of MIL-101(Fe) crystal was about 1 μm , which was consistent with the observation in SEM images.

The XRD patterns of MIL-101(Fe), g-C₃N₄, their physical mixture (g-C₃N₄ + MIL-101(Fe)), and MIL-101(Fe)/g-C₃N₄ heterojunction are presented in Fig. 1f. The characteristic diffraction peaks of the prepared heterojunction was analogous to those of the previously reported MIL-101(Fe) [48] and g-C₃N₄ [45], suggesting that the crystalline nature

MIL-101(Fe) was preserved in the heterojunction. However, the characteristic peak of g-C₃N₄, which was obviously presented in the mixture of g-C₃N₄ + MIL-101(Fe), was shifted to about half degree higher than that in the heterojunction, indicating strong coupling interaction between the two components in the heterojunction. The peak intensity of the mixture was weaker than that of MIL-101(Fe), because the MOF crystals in the mixture were partly sheltered by g-C₃N₄. This phenomenon was also observed in a MOF/graphene oxide composite [49]. The presence of g-C₃N₄ in the heterojunction can be validated by Raman spectra. As shown in Fig. S2, Raman signals of g-C₃N₄ can be clearly observed in MIL-101(Fe)/g-C₃N₄, and the signal intensity of g-C₃N₄ in the heterojunction was a little stronger in comparison with the pristine g-C₃N₄. This could be attributed to the surface-enhanced Raman scattering (SERS) effect from the contacted iron-MOF materials. An analogous enhanced effect was reported earlier in a Ag/g-C₃N₄ heterojunction [46].

Fig. 1g shows the FTIR spectra of MIL-101(Fe), g-C₃N₄, and MIL-101(Fe)/g-C₃N₄. The FTIR spectrum of g-C₃N₄ showed the characteristic peaks, such as N-H stretching vibrations (3000–3500 cm⁻¹), C-N heterocycle stretching modes (1635, 1544, 1398, 1315 and 1232 cm⁻¹), and the breathing mode of triazine units (806 cm⁻¹) [46]. However, no obvious absorption bands of g-C₃N₄ were found in MIL-101(Fe)/g-C₃N₄. Meanwhile, a significant decrease of the peak at 1683 cm⁻¹ for MIL-101(Fe)/g-C₃N₄ was observed in comparison with pristine MIL-101(Fe). This must be related to the interaction of MOF and g-C₃N₄. An analogous phenomenon was reported by Yang et al. [49]. The peak at 541 cm⁻¹ in both MIL-101(Fe) and MIL-101(Fe)/g-C₃N₄ heterojunction could be attributed to the Fe-O bond.

The EDS elemental distribution for MIL-101(Fe)/g-C₃N₄ is illustrated in Fig. 2. The elemental signal spots clearly showed that the

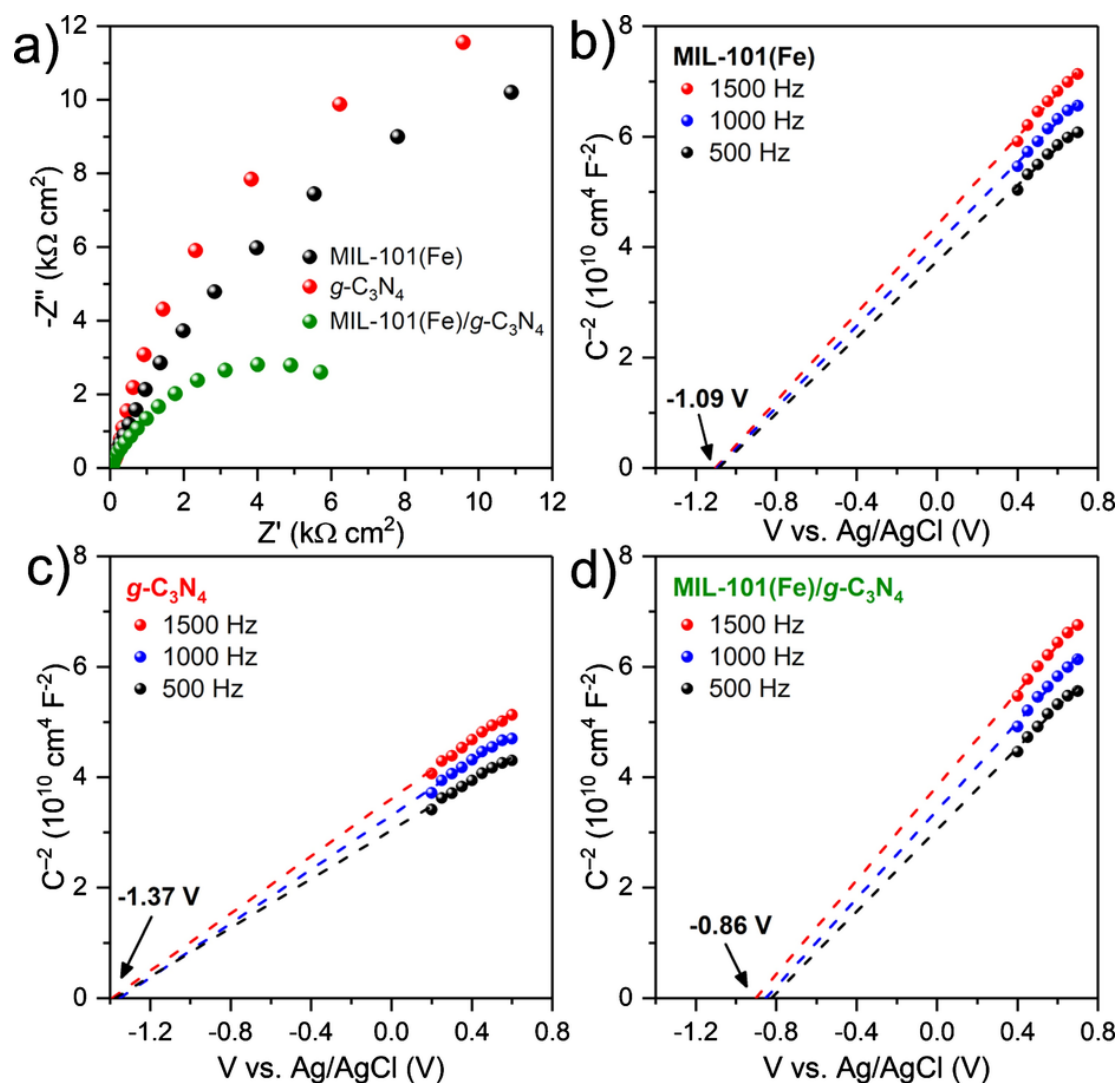


Fig. 6. Electrochemical impedance spectra of the three as-prepared samples (a). Typical Mott-Schottky plots of MIL-101(Fe) (b), $g\text{-C}_3\text{N}_4$ (c), and MIL-101(Fe)/ $g\text{-C}_3\text{N}_4$ (d) at different frequencies.

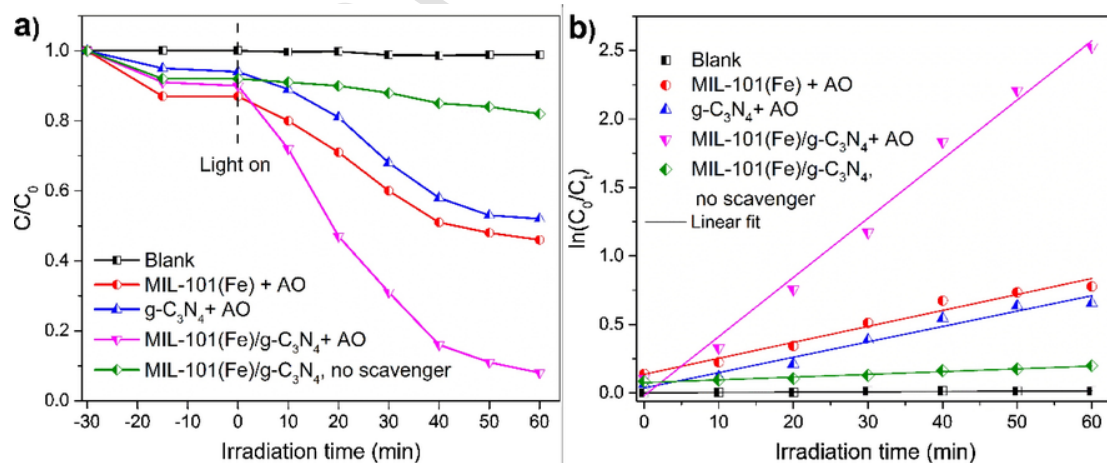


Fig. 7. Photocatalytic reduction of aqueous Cr(VI) by various photocatalysts (a), and the kinetics of Cr(VI) reduction by various photocatalysts (b). Reaction conditions: pH 5, 20 mg photocatalyst, 40 mL of 20 ppm Cr(VI), 5 mg $(\text{NH}_4)_2\text{C}_2\text{O}_4$ (AO, hole scavenger). Blank experiment: Cr(VI) + AO, no photocatalyst.

MOF crystals are well loaded on the surface of $g\text{-C}_3\text{N}_4$, since N is from $g\text{-C}_3\text{N}_4$ while O and Fe are from MIL-101(Fe). The EDS spectra quantitatively identified the presence of both $g\text{-C}_3\text{N}_4$ and MIL-101(Fe) in the

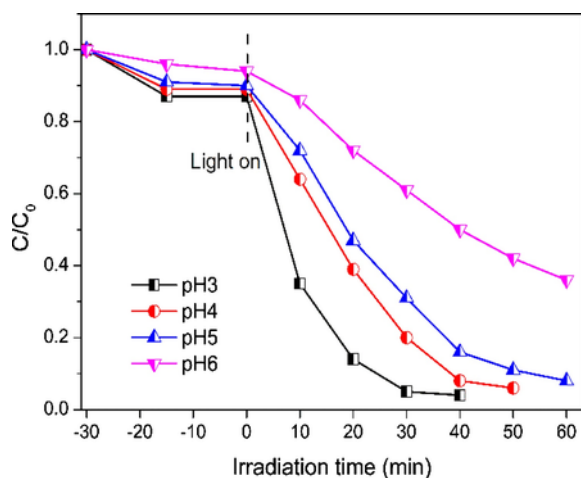


Fig. 8. Photocatalytic reduction of aqueous Cr(VI) by MIL-101(Fe)/g-C₃N₄ at different solution pHs. Reaction conditions: 20 mg photocatalyst, 40 mL of 20 ppm Cr(VI), 5 mg AO.

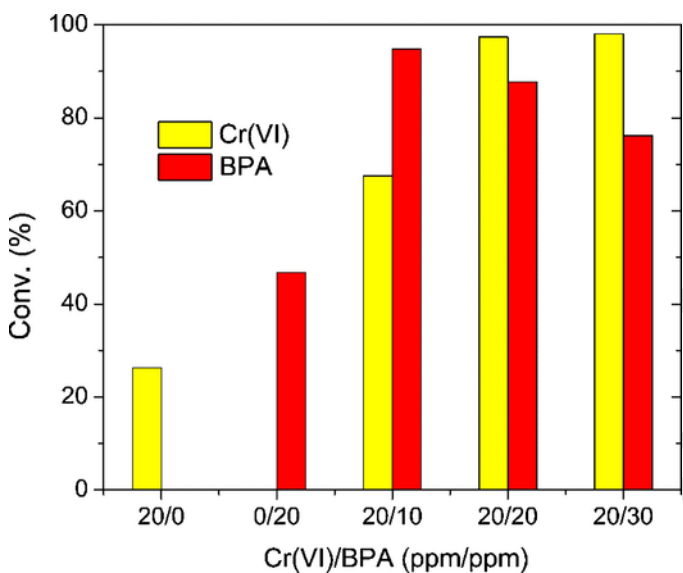


Fig. 9. Simultaneous photocatalytic reduction of Cr(VI) and degradation of BPA over MIL-101(Fe)/g-C₃N₄ at different initial concentration ratios under visible light irradiation. Reaction conditions: 20 mg photocatalyst, 40 mL of mixing solution, pH 6.8.

heterojunction (Inset Table, C: 37.22%, N: 13.80 wt.%, O: 28.12 wt.%, Fe: 16.83 wt.%).

Fig. 3 and Table 1 show the N₂ adsorption/desorption isotherms and pore size distributions of the as-prepared samples. As previously reported [34], pure g-C₃N₄ was considered as a non-porous material with low specific surface and poor porosity (Fig. 3 and Table 1). In the case of MIL-101(Fe) and MIL-101(Fe)/g-C₃N₄, both of them exhibited much higher specific surfaces and pore volumes in comparison with the reported MIL-53(Fe) (*S*_{BET} 20.6 m²/g, *V*_p 0.053 cm³/g) and MIL-53(Fe)/g-C₃N₄ (*S*_{BET} 18.5 m²/g, *V*_p 0.038 cm³/g) [51]. It is also noticed that both of the surface area and porosity of the g-C₃N₄ + MIL-101(Fe) mixture were much less than those of MIL-53(Fe)/g-C₃N₄ heterojunction, probably due to the heavy coverage of MOF porous structure by the g-C₃N₄ sheet in the physical mixture. A similar decrease trend was observed in MOF + graphene oxide mixture [49]. The parameters of MIL-53(Fe)/g-C₃N₄ are close to but still less than those of pristine MIL-53(Fe). Thus, the introduction of g-C₃N₄ in the precursor during the MOF synthesis does not prevent but still affect the formation of the porous structure [51]. TGA results (Fig. S3) show that MIL-53(Fe)/g-

C₃N₄ has better thermal stability than pristine MIL-53(Fe) in the temperature range from 30 to 550 °C, due to the introduction of g-C₃N₄ which is stable before 550 °C. The TG curve of MIL-53(Fe)/g-C₃N₄ was obviously different from MIL-53(Fe)/g-C₃N₄, indicating strong coupling interaction between the two components in the heterojunction.

The surface chemical compositions of the MOFs with and without g-C₃N₄ were analyzed by XPS. As shown in Fig. 4a, pristine MIL-101(Fe) did not display any signals in N 1s region. In contrast, the binding energy (BE) peaks from the N 1s at 396-402 eV existed in the spectrum of MIL-101(Fe)/g-C₃N₄ heterojunction, and the N content was estimated as 16.39%, further confirming the successful introduction of g-C₃N₄ in the heterojunction. Moreover, the two splitting BE peaks of N 1s at 400.8 and 398.6 eV (Fig. 4c), could be ascribed to C-NH_x and sp² hybridized N atoms in C = N, respectively [51]. The C 1s spectrum in Fig. 4b shows four BE peaks, where 284.0 and 285.4 eV could be assigned to sp²-bonded carbon C-C and C-N in g-C₃N₄, respectively [52], and 284.7 and 288.5 eV were corresponded to the benzoic rings and C = O of H₂BDC [48]. The O 1s spectrum could be fitted by two splitting peaks at around 531.8 and 530.2 eV (Fig. 4d), which could be attributed to the oxygen components of terephthalate linkers and Fe-O bonds of MIL-101(Fe), respectively [20,48]. The Fe 2p spectrum (Fig. 4e) shows two BE peaks at 711.9 and 725.6 eV ascribed to Fe 2p_{3/2} and Fe 2p_{1/2}, respectively. The peak separation (ΔBE between 2p_{3/2} and 2p_{1/2}) of 13.7 eV, together with the satellite peak at 716.4 eV, suggested the iron in the material is in the state of +3 [20]. All these XPS results confirmed the successful formation of MIL-101(Fe)/g-C₃N₄ heterojunction.

The optical absorption property of a semiconductor decides its photocatalytic activity. Therefore, UV-DRS analyses of MIL-101(Fe) and g-C₃N₄ materials were conducted, and the results are shown in Fig. 5a. The pristine g-C₃N₄ can absorb visible light and exhibits yellow color. Based on the Kubelka-Munk plots (Fig. 5b), the estimated bandgap of g-C₃N₄ is 2.70 eV, which is in a good agreement with the previous report [31]. In comparison with pristine g-C₃N₄, pure MIL-101(Fe) exhibits stronger visible light absorption in the range of 400-600 nm and shows orange color. After the incorporation of g-C₃N₄, the visible light absorption was significantly enhanced in MIL-101(Fe)/g-C₃N₄ composite. However, the visible light absorption of physically mixed g-C₃N₄ + MIL-101(Fe) was significantly weaker than that of MIL-101(Fe)/g-C₃N₄. This also implies that the formation of heterojunction between MIL-101(Fe) and g-C₃N₄ will play roles in the enhancement of visible-light absorption due to the interaction between the both components. Importantly, it is noted that a red shift of the absorption band edge occurred after the introduction of g-C₃N₄ in the composite, indicating the narrower bandgap of the MIL-101(Fe)/g-C₃N₄ heterojunction. Based on the Kubelka-Munk plots (Fig. 5b), the bandgaps of the pristine MIL-101(Fe) and MIL-101(Fe)/g-C₃N₄ were estimated as 2.54 eV and 2.26 eV, respectively. Similar enhancements of the absorptivity in visible-light region have also been observed in the reported heterojunction of other MOFs with rGO [49] and g-C₃N₄ [51]. The enhanced visible light absorption was reported to be beneficial to improve photocatalytic efficiency in those works.

Photoluminescence (PL) analysis has been widely used to investigate the separation efficiency of the photon-induced electron-hole pairs in photocatalysts. The PL emission peaks are correlated to electron-hole recombination. A higher emission intensity corresponds to the severer electron-hole pair recombination [53]. Fig. 5c illustrates the PL spectra of g-C₃N₄, MIL-101(Fe) and MIL-101(Fe)/g-C₃N₄ composites. g-C₃N₄ shows the highest PL emission intensity, which means the highest recombination between the photogenerated electrons and holes. However, after the incorporation of MIL-101(Fe), the MIL-101(Fe)/g-C₃N₄ composite presents a much lower PL peak intensity than that of pristine g-C₃N₄, indicating the decreased recombination of photogenerated electron-hole pairs in the MIL-101(Fe)/g-C₃N₄ system. The PL analyses

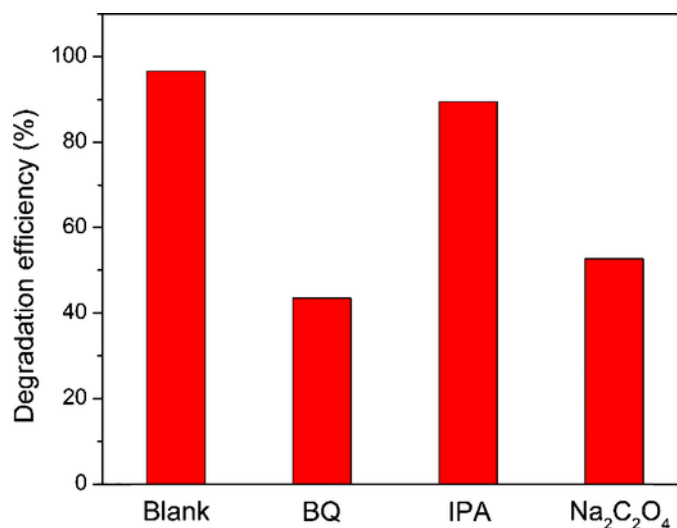


Fig. 10. Photocatalytic degradation of BPA by MIL-101(Fe)/g-C₃N₄ in the presence of different scavengers under visible-light irradiation.

reveal that the introduction of MIL-101(Fe) could efficiently enhance the separation of the photon-generated electron-hole pairs and thus improve the photocatalytic activity [49].

For the investigation of the band structures of the materials, the valence band edges (E_{VB}) of MIL-101(Fe) and g-C₃N₄ were measured by performing the valence-band X-ray photoelectron spectroscopy (VB-XPS) measurements. As shown in Fig. 5d, the valence band edges of pristine MIL-101(Fe) and g-C₃N₄ were observed at 2.50 eV and 1.62 eV, respectively. These E_{VB} values are consistent with the previously reported results [40,54]. Based on these E_{VB} values and the bandgap results obtained by UV-DRS (Fig. 5a, b), the conduction band edges (E_{CB}) could be calculated by the following equation.

$$E_{CB} = E_{VB} - E_g \quad (1)$$

Accordingly, the E_{CB} values of g-C₃N₄ and MIL-101(Fe) are calculated to be -1.08 V and -0.04 V vs. NHE, respectively. Importantly, both the CB and VB edges of MIL-101(Fe) are lower than those of g-C₃N₄, suggesting a direct Z-scheme heterojunction formation of MIL-101(Fe)/g-C₃N₄. More significantly, both of the CB values of MIL-101(Fe) and g-C₃N₄ are more negative than the Cr(VI)/Cr(III) potential (+0.51 V vs. NHE) [51]. Therefore, it is thermodynamically feasible to reduce Cr(VI) into Cr(III) on the CB of the heterojunction during the photocatalytic process.

To gain insights into the interfacial charge carrier behaviors and band structure, we carried out the EIS measurements in 0.5 M Na₂SO₄ solution containing H₂O₂ sacrificial agent under dark condition. Representative Nyquist plots of the impedance response are displayed in Fig. 6a, where deformed semicircle is shown in all cases. The size of the semicircle, which correlates with interfacial charge transport resistance (the larger the semicircle, the higher the resistance) [55,56], shows a clear trend among the three different samples. Both MIL-101(Fe) and g-C₃N₄ exhibit a high charge transport resistance where g-C₃N₄ is slightly less resistive than MIL-101(Fe). As expected, g-C₃N₄/MIL-101(Fe) heterojunctions demonstrate the lowest charge transport resistance, which reveals the formation of heterojunctions facilitate the charge transport process from the photocatalyst to electrolyte. These impedance results are consistent with PL analysis, indicating the introduction of g-C₃N₄ on MIL-101(Fe) effectively suppresses the charge recombination process. The fact that heterojunction formation facilitates charge transport and passivates surface recombination has also been recently reported on other photocatalytic systems [57]. We then take a step further and perform Mott-Schottky analysis on MIL-101(Fe) (Fig. 6b), g-C₃N₄ (Fig. 6c) and MIL-101(Fe)/g-C₃N₄ (Fig. 6d). In all the cases, the

Mott-Schottky plot shows a positive slope which confirms the n-type character of these three samples. By fitting the linear region of the Mott-Schottky plot, flat band potential (E_{FB}) can be determined at the y-intercept [58]. The g-C₃N₄ shows the most negative E_{FB} with a value around -1.37 V vs Ag/AgCl, which is in line with that of mesoporous g-C₃N₄ [59]. Likewise, MIL-101(Fe) exhibits a E_{FB} value of -1.09 V vs Ag/AgCl, which is around 200 mV more negative than that of a MIL-68(Fe) photocatalyst [21]. Compared with pristine MIL-101(Fe), g-C₃N₄/MIL-101(Fe) heterojunctions demonstrate a positive shift of E_{FB} around 230 mV, which is a sign that g-C₃N₄/MIL-101(Fe) will exhibit a higher oxidation ability than bare MIL-101(Fe). A similar behavior has been found on MIL-68(In)-NH₂/rGO photocatalytic systems, recently reported by Yang et al [49].

3.2. Photocatalytic performance

The photocatalytic performance of the as-prepared MIL-101(Fe)/g-C₃N₄ was firstly investigated by Cr(VI) reduction in water under visible light illumination. The control experiment was carried out to exclude the natural photolysis. As shown in Fig. 7a, no significant Cr(VI) reduction was observed in the absence of a photocatalyst (the black curve in Fig. 7a), indicating that Cr(VI) does not react with the hole scavenger in the absence of photocatalysts. The efficient adsorption of Cr(VI) onto TiO₂ was observed in a previously reported investigation [60], thus the dark adsorption of Cr(VI) onto the studied adsorbents was also investigated. In dark conditions, all the three materials could adsorb certain amounts of Cr(VI) (12.6% for MIL-101(Fe), 6.2% for g-C₃N₄ and 10.5% for MIL-101(Fe)/g-C₃N₄, respectively) and reach equilibrium in 30 min. Under visible light illumination, the reduction reaction proceeded smoothly in the presence of photocatalysts and hole scavenger. After illumination for 60 min, the reduction ratios of Cr(VI) reached 53.8%, 48.1%, and 92.6% for MIL-101(Fe), g-C₃N₄, and MIL-101(Fe)/g-C₃N₄, respectively. Notably, the MIL-101(Fe)/g-C₃N₄ composite possessed significantly higher photocatalytic performance compared to the pristine MIL-101(Fe) and g-C₃N₄. To investigate the effect of the hole scavenger, we conducted a control experiment by using MIL-101(Fe)/g-C₃N₄ photocatalyst in the absence of ammonium oxalate (AO). It was found that the reduction of Cr(VI) hardly occurred in the absence of the hole scavenger (the green curve in Fig. 7a). These results indicated that the reduction is a photocatalytic driven process and the light, photocatalyst, and scavenger act important roles in the photocatalytic process. For the photocatalytic reduction of Cr(VI), AO serves as a hole scavenger, which could capture the photogenerated holes (h^+) from

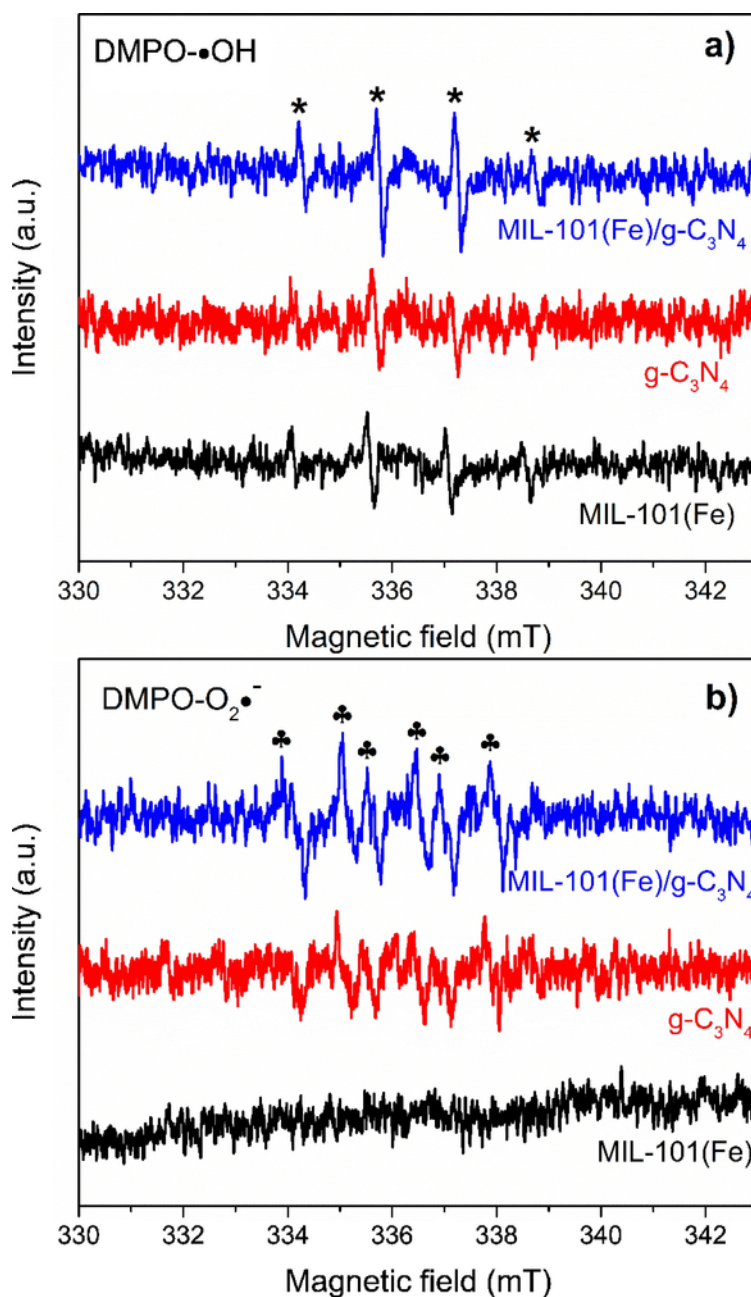


Fig. 11. ESR spectra of the DMPO-OH a) and DMPO-O₂•⁻ b) for MIL-101(Fe), g-C₃N₄ and MIL-101(Fe)/g-C₃N₄ after 60 s of visible light irradiation.

the photocatalyst, mitigating the recombination of photoinduced e⁻/h⁺. Fig. 7b presents the kinetic fitting curves for the Cr(VI) reduction by different photocatalysts. The perfect linear fitting (Fig. 7b) and high R^2 values (Table S1) suggest that the reduction follows the pseudo-first-order kinetics [61]. As presented in Table S1, the photocatalytic Cr(VI) reduction rate constant of MIL-101(Fe)/g-C₃N₄ was almost 3.7 times higher than the pristine MIL-101(Fe) and 3.9 times higher than the pure g-C₃N₄. All these results can prove that the photocatalytic activity of MIL-101(Fe) was enhanced through the incorporation of g-C₃N₄.

In the photocatalytic reduction of aqueous Cr(VI), an optimum pH is important. The influence of pH on the Cr(VI) reduction by MIL-101(Fe)/g-C₃N₄ was then studied in a pH range of 3-6 (Fig. 8). Alkaline solutions were not used to avoid the hydroxide formation of reduced chromium (Cr(OH)₃) [62]. Similar to other MOF photocatalysts

[21,63], the photocatalytic reduction activity of MIL-101(Fe)/g-C₃N₄ was found to be dependent on the solution pH. From pH 6 to 3, the reduction ratio increased with decreasing pH (67.2% at pH 6, 92.6% at pH 5, 93.8% at pH 4, and 98.1% at pH 3, respectively). Notably, the almost 100% reduction ratio at pH 3 was achieved within only 30 min of visible light irradiation. These results reveal that more acidic media favored the photocatalysis over MIL-101(Fe)/g-C₃N₄. For better understanding of this phenomenon, the surface zeta potentials (ζ) of MIL-101(Fe) and MIL-101(Fe)/g-C₃N₄ at various pHs were examined (Fig. S4). The isoelectric points were determined to be 7.6 and 6.8 for MIL-101(Fe) and MIL-101(Fe)/g-C₃N₄, respectively. This indicates positively charged surface of MIL-101(Fe)/g-C₃N₄ in water at pH < 6.8, while the dominated species of Cr(VI) are Cr₂O₇²⁻ anionic ions [20]. At pH < 6.8, a lower pH value corresponds more positively charged surface of MIL-101(Fe)/g-C₃N₄, resulting in better adsorption of Cr₂O₇²⁻ anionic ions and favorable reduction.

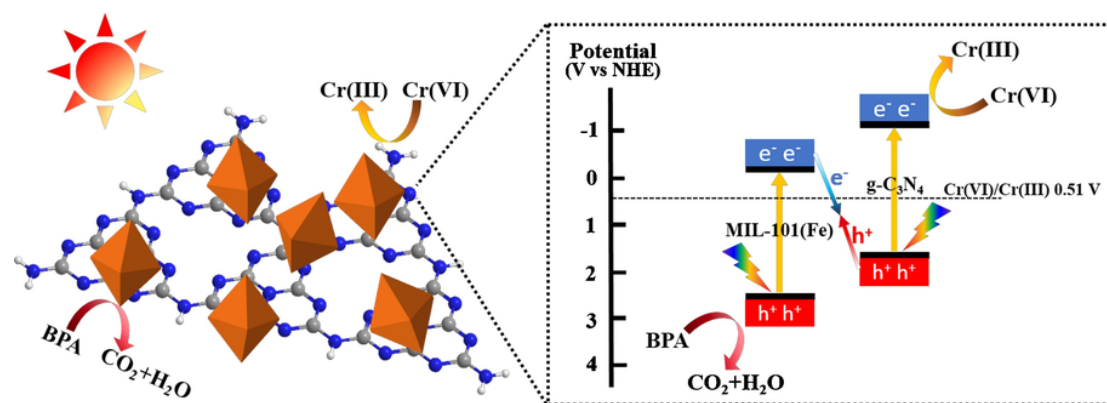


Fig. 12. Schematic illustration of the simultaneous photocatalytic reduction of Cr(VI) and oxidation of BPA over a direct Z-scheme MIL-101(Fe)/g-C₃N₄ heterojunction under visible light irradiation.

As we know, heavy metals are often discharged together with other hazardous organic pollutants (such as bisphenols) in industrial wastewater [2]. In this study, we simulated bi-component systems containing 20 mg/L Cr(VI) and a certain concentration (10/20/30 mg/L) of BPA at natural pH (ca. 6.8) without adding any other hole scavenger to evaluate the photocatalytic performance of MIL-101(Fe)/g-C₃N₄ in the treatment of different categories of pollutants simultaneously. As shown in Fig. 9, in the case of single Cr(VI) system without any organic compound (20/0), the reduction efficiency was relatively low (only 26.2%) after 4 h of continuous reaction under visible light irradiation, which could be attributed to the absence of a hole scavenger. By contrast, in the presence of BPA, the reduction efficiency of Cr(VI) was significantly increased. In the binary systems of Cr(VI)/BPA of 20/10, 20/20, 20/30, the reduction efficiencies of Cr(VI) were 68.0%, 97.1%, and 98.8%, respectively. Meanwhile, the presence of Cr(VI) could also enhance the photocatalytic oxidation of BPA in the binary systems. In the single system, the photodegradation efficiency of BPA was 46.6%. The photocatalytic degradation of BPA was dramatically promoted to 94.8%, 87.7%, and 76.2% in binary systems. The enhanced photocatalytic performance of MIL-101(Fe)/g-C₃N₄ in the binary systems could be ascribed to the synergistic effect between the photocatalytic reduction and oxidation process. In the binary system, BPA serves as a photogenerated hole scavenger and is oxidized, while Cr(VI) acts as a photogenerated electron acceptor and is reduced. The mineralization of total organic carbon (TOC) was also determined (Fig. S5). It was observed that the TOC trend (Fig. S5) was similar to the BPA degradation trend (Fig. 9). The presence of Cr(VI) promoted dramatically the BPA mineralization from 37.5% (Cr(VI)/BPA: 0/20) to 56.6% (Cr(VI)/BPA: 20/20). However, when the concentration of BPA increased from 10 to 30 ppm, the mineralization efficiency of TOC decreased from 62.7% to 48.2%. This might be due to the excessive molar extinction coefficient of BPA, resulting in lower efficiencies of light utilization [64].

3.3. Possible mechanisms of photocatalysis

The trapping experiments of radical species ($\bullet\text{OH}$, $\text{O}_2\bullet^-$ and h^+) and the ESR analyses were carried out to explore the mechanism of MIL-101(Fe)/g-C₃N₄ for the simultaneous degradation of BPA and reduction of Cr(VI) in aqueous solution. In the trapping experiments, BQ/IPA/Na₂C₂O₄ were used as the scavengers of $\text{O}_2\bullet^-/\bullet\text{OH}/\text{h}^+$, respectively [35] to determine the active species in the photocatalytic process. Fig. 10 shows the degradation efficiency of BPA over MIL-101(Fe)/g-C₃N₄ in the presence of the different scavengers. It is clearly observed that BQ and Na₂C₂O₄ had more significant effects on the photocatalytic performance of MIL-101(Fe)/g-C₃N₄, which reveals that $\text{O}_2\bullet^-$ and h^+ play more important roles in the photocatalytic oxidation process than $\bullet\text{OH}$. This could be attributed to the fact that $\bullet\text{OH}$ is mainly generated

through the oxidation of water by h^+ as Eq. 1 [65]. Therefore, if h^+ was scavenged, the generation of $\bullet\text{OH}$ would be greatly reduced.



ESR analyses were applied to verify the existence of $\bullet\text{OH}$ and $\text{O}_2\bullet^-$ radicals in the photocatalytic process of MIL-101(Fe), g-C₃N₄, and MIL-101(Fe)/g-C₃N₄. Fig. 11a shows the ESR signals of DMPO- $\bullet\text{OH}$ over the three as-prepared samples. The four characteristic peaks of the DMPO- $\bullet\text{OH}$ adducts could be clearly observed in all the samples, indicating that the $\bullet\text{OH}$ radicals were produced in all the photocatalytic systems in this study. It is worth to notice that MIL-101(Fe) possessed relatively stronger signals than that of g-C₃N₄. This might be because more positive VB potential (E_{VB}) of MIL-101(Fe) (2.50 eV) than that of g-C₃N₄ (1.62 eV), which is theoretically beneficial to the generation of h^+ , resulting in higher production of $\bullet\text{OH}$ according to Eq. 1 [49]. In Fig. 11b, six characteristic peaks of the DMPO- $\text{O}_2\bullet^-$ adducts were obviously observed for both of g-C₃N₄ and MIL-101(Fe)/g-C₃N₄, indicating that the $\text{O}_2\bullet^-$ radicals were generated after 60 s of visible light irradiation by these two samples [66]. The $\text{O}_2\bullet^-$ signal of g-C₃N₄ was much stronger than that of bare MIL-101(Fe), since the CB potential (E_{CB}) of g-C₃N₄ (-1.08 eV) is more negative than that of the MIL-101(Fe) (-0.04 eV), which is favorable to the generation of photo-induced e^- for the reduction of O_2 as follows [67].

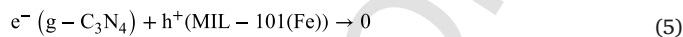
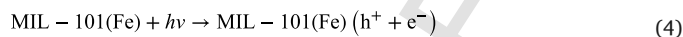
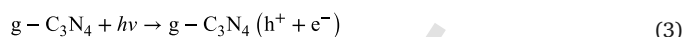


Obviously, the ESR signals of both DMPO- $\bullet\text{OH}$ and DMPO- $\text{O}_2\bullet^-$ in MIL-101(Fe)/g-C₃N₄ heterojunction were much stronger than those in both pristine MIL-101(Fe) and bare g-C₃N₄, indicating that the separation efficiency of photo-induced h^+/e^- pairs in MIL-101(Fe)/g-C₃N₄ heterojunction was significantly higher than those of single MIL-101(Fe) and g-C₃N₄. Overall, ESR experiments showed that the transfer of electrons from the as-prepared heterojunction to O_2 is important to produce $\text{O}_2\bullet^-$, which is useful for the photocatalytic oxidation of organic pollutants [68]. To further verify this oxygen-induced radical reaction, we investigated the photocatalytic degradation of BPA by MIL-101(Fe)/g-C₃N₄ at different O_2 concentrations. The continuous nitrogen aeration, which could expel oxygen out of the solution, was applied as 0% oxygen condition. As shown in Fig. S6, the photocatalytic degradation activity of MIL-101(Fe)/g-C₃N₄ was found to be dependent on the O_2 concentration. From N_2 aeration to air and then to pure O_2 aeration, the BPA degradation efficiency increased with increasing O_2 concentration (37.3% at 0% O_2 , 91.2% at 20% O_2 , and 96.4% at 100% O_2 , respectively). Notably, almost 100% degradation at pure O_2 aeration was achieved within 30 min of visible light irradiation. These results reveal that oxygen played a significant role in the photocatalysis and higher O_2 concentration favored the photocatalytic degradation of

BPA over MIL-101(Fe)/g-C₃N₄. From ESR and O₂ concentration experiments, it can be concluded that the photocatalytic oxidation of organic pollutants is a typical oxygen-induced radical pathway. Moreover, the generated electrons are also available for other reduction reactions such as the reduction of Cr(VI). On the other hand, the presence of •OH verifies the successful generation of h⁺ in the photocatalytic system of the heterojunction. Both h⁺ and •OH are the typical species for the photocatalytic oxidation of organic pollutants [35,69].

From the Mott-Schottky experiments, UV-vis DRS spectra, and VB-XPS spectra, the E_{VB} edges of pristine MIL-101(Fe) and g-C₃N₄ were observed at 2.50 V and 1.62 V vs NHE, respectively, while the E_{CB} values of MIL-101(Fe) and g-C₃N₄ were calculated to be -0.04 V and -1.08 V vs NHE, respectively. When MIL-101(Fe) is anchored on g-C₃N₄ surface in a close contact, the electrons in g-C₃N₄ spontaneously transfer to MIL-101(Fe) across the interface until their Fermi levels are equal, resulting in inner electrical fields in the direction from g-C₃N₄ to MIL-101(Fe) [70,71]. Under visible light irradiation, the electrons are excited from VB to CB of both MIL-101(Fe) and g-C₃N₄. The charge transfer at the interfacial phases may follow double-transfer mechanism (Fig. S7a) or direct Z-scheme mechanism (Fig. S7b). The direction of the photogenerated charge across the MIL-101(Fe)/g-C₃N₄ heterojunctions can be inferred by combining the ESR results with the established band alignment [72,73]. As shown in Fig. 11a, The DMPO-•OH signals of MIL-101(Fe) and MIL-101(Fe)/g-C₃N₄ could be observed, while very weak DMPO-•OH signal was observed for pure g-C₃N₄. The weak signal of DMPO-•OH in g-C₃N₄ was due to the weak oxidation potential of photogenerated holes (Eq. (1)) in g-C₃N₄ (1.62 V vs NHE). The observation of DMPO-•OH signal in MIL-101(Fe)/g-C₃N₄ composite indicates that the photogenerated holes still stay in the VB of MIL-101(Fe) and do not transfer to the VB of g-C₃N₄. Similarly, as shown in Fig. 11b, strong DMPO-O₂•⁻ signals were observed for both g-C₃N₄ and MIL-101(Fe)/g-C₃N₄, whereas almost no obvious DMPO-O₂•⁻ signal could be observed for MIL-101(Fe). The absence of DMPO-O₂•⁻ signal in MIL-101(Fe) was due to the weak reduction potential of photogenerated electrons (Eq. (2)) in MIL-101(Fe) (-0.04 V vs NHE). The results indicate that the photogenerated electrons in g-C₃N₄ and MIL-101(Fe)/g-C₃N₄ have enough reduction ability to reduce O₂ to form superoxide radical anions (O₂•⁻) (Eq. (2)) [74]. The above ESR results indicate that the photogenerated electrons and holes are present in the CB of g-C₃N₄ and VB of MIL-101(Fe), respectively, and the charge transfer does not follow the conventional double-transfer mechanism. In contrast, the direct Z-scheme mechanism can better explain the enhancement of photocatalytic reduction of Cr(VI) in MIL-101(Fe)/g-C₃N₄ [75][71]. Similar ESR behaviors have been observed in WO₃/g-C₃N₄[74], m-Bi₂O₄/g-C₃N₄ [76], TiO₂/g-C₃N₄ [77] step-scheme (Z-scheme or S-scheme) photocatalysts. Based on the ESR results and band alignment, the schematic illustration of the band structure diagram and charge transport route of MIL-101(Fe)/g-C₃N₄ heterojunction is shown in Fig. 12. The relative band alignment between MIL-101(Fe) and g-C₃N₄ allows the formation of a direct Z-scheme heterojunction [71][78]. In such a MIL-101(Fe)/g-C₃N₄ system, photogenerated electrons in the CB of MIL-101(Fe) recombine with photogenerated holes in the VB of g-C₃N₄ (Eq. (5)) [51], while photogenerated electrons with a strong reduction ability remained in the CB of g-C₃N₄ are ready to reduce Cr(VI) into Cr(III) (Eq. (6)) and photogenerated holes with strong oxidation abilities in the VB of MIL-101(Fe) could promote the oxidation of organic pollutants such as BPA (Eq. (7)) [79]. Therefore, the formation of a direct Z-scheme MIL-101(Fe)/g-C₃N₄ heterojunction can drive photogenerated carriers with strong redox abilities to perform photocatalytic reactions [80]. The aforementioned direct Z-scheme mechanism could effectively mitigate the charge recombination inside each semiconductor, and thus obtain superior photocatalytic performance thanks to photogenerated carriers with strong redox abilities. Consequently, the effective separation of photo-induced h⁺/e⁻ pairs leads to an enhanced

photocatalytic performance of MIL-101(Fe)/g-C₃N₄ heterojunction for the simultaneous photocatalytic reduction of Cr(VI) and oxidation of BPA.



4. Conclusions

In summary, visible-light-driven simultaneous treatment of Cr(VI) and bisphenol A (BPA) is realized over MIL-101(Fe)/g-C₃N₄ composites synthesized via a facile in-situ solvothermal synthesis approach. UV-vis DRS verified that the MIL-101(Fe)/g-C₃N₄ composites possess enhanced photo-absorption properties in comparison with the pristine MIL-101(Fe). The photocatalytic results reveal that the acidic media was favorable to the reduction of Cr(VI). Moreover, the addition of BPA could enhance the photocatalytic reduction of Cr(VI) because BPA could act as hole scavengers to improve the separation of photo-induced charge carriers. The radical species trapping and ESR results showed that photo-generated electrons are responsible for the reduction of Cr(VI) and the BPA degradation followed an oxygen-induced pathway. By virtue of the advantages of enhanced light absorption, efficient charge carrier separation, as well as the matching band potentials between the two components, the heterojunction exhibited remarkably improved photocatalytic activities in the reduction of Cr(VI) and degradation of BPA. The introduction of g-C₃N₄ into MIL-101(Fe) not only increased light absorption, but also greatly enhanced interfacial charge carrier separation by forming a direct Z-scheme heterojunction with appropriate band alignment, thus resulting in the superior activities for Cr(VI) reduction and BPA degradation. These findings provide a promising strategy for designing high-efficiency metal-free semiconductor/Fe-based MOFs heterojunctions with outstanding photocatalytic performance for simultaneous removal of different pollutants.

5. Declaration of Competing Interest

The authors declare that they have no known competing financial interests or personal relationships that could have appeared to influence the work reported in this paper.

Uncited References

[26,78].

CRedit authorship contribution statement

Feiping Zhao: Data curation, Writing - original draft. **Shaobin Wang:** Data curation, Writing - review & editing.

Acknowledgments

The authors are grateful to the European Regional Development Fund (iFORMINE), National Science Fund for Distinguished Young Scholars (No. 51825403), Key R&D Program of Hunan Province (2018SK2044) and the Australian Research Council (DP170104264) for financial support. Y. L. and N. G. thank the Swiss

National Science Foundation (SNF) for funding support under the Ambizione Energy grant no. PZENP2_166871. We also thank anonymous reviewers for their constructive comments and suggestions.

Appendix A. Supplementary data

Supplementary material related to this article can be found, in the online version, at doi:<https://doi.org/10.1016/j.apcatb.2020.119033>.

References

- J. Hu, G. Chen, I.M.C. Lo, Removal and recovery of Cr(VI) from wastewater by maghemite nanoparticles, *Water Research*. 39 (2005) 4528–4536, <https://doi.org/10.1016/j.watres.2005.05.051>.
- F. Zhao, E. Repo, D. Yin, Y. Meng, S. Jafari, M. Sillanpää, EDTA-Cross-Linked β -Cyclodextrin: An Environmentally Friendly Bifunctional Adsorbent for Simultaneous Adsorption of Metals and Cationic Dyes, *Environmental Science & Technology*. 49 (2015) 10570–10580, <https://doi.org/10.1021/acs.est.5b02227>.
- F. Zhao, E. Repo, D. Yin, L. Chen, S. Kalliola, J. Tang, E. Iakovleva, K.C. Tam, M. Sillanpää, One-pot synthesis of trifunctional chitosan-EDTA- β -cyclodextrin polymer for simultaneous removal of metals and organic micropollutants, *Scientific Reports*. 7 (2017) 1–14, <https://doi.org/10.1038/s41598-017-16222-7>.
- Y. Orojji, M. Ghanbari, O. Amiri, M. Salavati-Niasari, Facile fabrication of silver iodide/graphitic carbon nitride nanocomposites by notable photo-catalytic performance through sunlight and antimicrobial activity, *Journal of Hazardous Materials*. 389 (2020) 122079, <https://doi.org/10.1016/j.jhazmat.2020.122079>.
- L.B. Khalil, W.E. Mourad, M.W. Rophael, Photocatalytic reduction of environmental pollutant Cr(VI) over some semiconductors under UV/visible light illumination, *Applied Catalysis B: Environmental*. 17 (1998) 267–273, [https://doi.org/10.1016/S0926-3373\(98\)00020-4](https://doi.org/10.1016/S0926-3373(98)00020-4).
- M. Ghanbari, M. Bazarganipour, M. Salavati-Niasari, Photodegradation and removal of organic dyes using CuI nanostructures, green synthesis and characterization, *Separation and Purification Technology*. 173 (2017) 27–36, <https://doi.org/10.1016/j.seppur.2016.09.003>.
- J. Yu, W. Wang, B. Cheng, B.-L. Su, Enhancement of Photocatalytic Activity of Mesoporous TiO₂ Powders by Hydrothermal Surface Fluorination Treatment, *The Journal of Physical Chemistry C*. 113 (2009) 6743–6750, <https://doi.org/10.1021/jp900136q>.
- M. Shekofteh-Gohari, A. Habibi-Yangjeh, M. Abitorabi, A. Rouhi, Magnetically separable nanocomposites based on ZnO and their applications in photocatalytic processes: A review, *Critical Reviews in Environmental Science and Technology*. 48 (2018) 806–857, <https://doi.org/10.1080/10643389.2018.1487227>.
- S. Zinatloo-Ajabshir, M. Salavati-Niasari, Facile route to synthesize zirconium dioxide (ZrO₂) nanostructures: Structural, optical and photocatalytic studies, *Journal of Molecular Liquids*. 216 (2016) 545–551, <https://doi.org/10.1016/j.molliq.2016.01.062>.
- J.A. Navío, G. Colón, M. Trillas, J. Peral, X. Domènech, J. Testa, J. Padrón, D. Rodríguez, M. Litter, Heterogeneous photocatalytic reactions of nitrite oxidation and Cr(VI) reduction on iron-doped titania prepared by the wet impregnation method, *Applied Catalysis B: Environmental*. 16 (1998) 187–196, [https://doi.org/10.1016/S0926-3373\(97\)00073-8](https://doi.org/10.1016/S0926-3373(97)00073-8).
- X. Liu, L. Pan, Q. Zhao, T. Lv, G. Zhu, T. Chen, T. Lu, Z. Sun, C. Sun, UV-assisted photocatalytic synthesis of ZnO-reduced graphene oxide composites with enhanced photocatalytic activity in reduction of Cr(VI), *Chemical Engineering Journal*. 183 (2012) 238–243, <https://doi.org/10.1016/j.cej.2011.12.068>.
- H. Fu, G. Lu, S. Li, Adsorption and photo-induced reduction of Cr(VI) ion in Cr(VI)-4CP (4-chlorophenol) aqueous system in the presence of TiO₂ as photocatalyst, *Journal of Photochemistry and Photobiology A: Chemistry*. 114 (1998) 81–88, [https://doi.org/10.1016/S1010-6030\(98\)00205-6](https://doi.org/10.1016/S1010-6030(98)00205-6).
- H.-C. Zhou, J.R. Long, O.M. Yaghi, Introduction to Metal–Organic Frameworks, *Chemical Reviews*. 112 (2012) 673–674, <https://doi.org/10.1021/cr300014x>.
- R.N. Widmer, G.I. Lampronti, S. Anzellini, R. Gaillac, S. Farsang, C. Zhou, A.M. Belenguer, C.W. Wilson, H. Palmer, A.K. Kleppe, M.T. Wharmby, X. Yu, S.M. Cohen, S.G. Telfer, S.A.T. Redfern, F.-X. Coudert, S.G. MacLeod, T.D. Bennett, Pressure promoted low-temperature melting of metal–organic frameworks, *Nature Materials*. 18 (2019) 370–376, <https://doi.org/10.1038/s41563-019-0317-4>.
- H.S. Quah, W. Chen, M.K. Schreyer, H. Yang, M.W. Wong, W. Ji, J.J. Vittal, Multi-photon harvesting metal–organic frameworks, *Nature Communications*. 6 (2015) 7954, <https://doi.org/10.1038/ncomms8954>.
- S. Abedi, A. Morsali, Ordered Mesoporous Metal–Organic Frameworks Incorporated with Amorphous TiO₂ As Photocatalyst for Selective Aerobic Oxidation in Sunlight Irradiation, *ACS Catalysis*. 4 (2014) 1398–1403, <https://doi.org/10.1021/cs500123d>.
- F.X. Llabrés i Xamena, A. Corma, H. Garcia, Applications for Metal–Organic Frameworks (MOFs) as Quantum Dot Semiconductors, *The Journal of Physical Chemistry C*. 111 (2007) 80–85, <https://doi.org/10.1021/jp063600e>.
- L. Shen, S. Liang, W. Wu, R. Liang, L. Wu, Multifunctional NH₂-mediated zirconium metal–organic framework as an efficient visible-light-driven photocatalyst for selective oxidation of alcohols and reduction of aqueous Cr(vi), *Dalton Transactions*. 42 (2013) 13649, <https://doi.org/10.1039/c3dt51479j>.
- R. Liang, L. Shen, F. Jing, W. Wu, N. Qin, R. Lin, L. Wu, NH₂-mediated indium metal–organic framework as a novel visible-light-driven photocatalyst for reduction of the aqueous Cr(VI), *Applied Catalysis B: Environmental*. 162 (2015) 245–251, <https://doi.org/10.1016/j.apcatb.2014.06.049>.
- R. Liang, F. Jing, L. Shen, N. Qin, L. Wu, MIL-53(Fe) as a highly efficient bifunctional photocatalyst for the simultaneous reduction of Cr(VI) and oxidation of dyes, *Journal of Hazardous Materials*. 287 (2015) 364–372, <https://doi.org/10.1016/j.jhazmat.2015.01.048>.
- F. Jing, R. Liang, J. Xiong, R. Chen, S. Zhang, Y. Li, L. Wu, MIL-68(Fe) as an efficient visible-light-driven photocatalyst for the treatment of a simulated waste-water contain Cr(VI) and Malachite Green, *Applied Catalysis B: Environmental*. 206 (2017) 9–15, <https://doi.org/10.1016/j.apcatb.2016.12.070>.
- N. Liu, W. Huang, X. Zhang, L. Tang, L. Wang, Y. Wang, M. Wu, Ultrathin graphene oxide encapsulated in uniform MIL-88A(Fe) for enhanced visible light-driven photodegradation of RhB, *Applied Catalysis B: Environmental*. 221 (2018) 119–128, <https://doi.org/10.1016/j.apcatb.2017.09.020>.
- Y. Fang, J. Wen, G. Zeng, F. Jia, S. Zhang, Z. Peng, H. Zhang, Effect of mineralizing agents on the adsorption performance of metal–organic framework MIL-100(Fe) towards chromium(VI), *Chemical Engineering Journal*. 337 (2018) 532–540, <https://doi.org/10.1016/j.cej.2017.12.136>.
- C.-C. Wang, X.-D. Du, J. Li, X.-X. Guo, P. Wang, J. Zhang, Photocatalytic Cr(VI) reduction in metal–organic frameworks: A mini-review, *Applied Catalysis B: Environmental*. 193 (2016) 198–216, <https://doi.org/10.1016/j.apcatb.2016.04.030>.
- D.A. Giannakoudakis, N.A. Travlou, J. Secor, T.J. Bandosz, Oxidized g-C₃N₄ Nanospheres as Catalytically Photoactive Linkers in MOF/g-C₃N₄ Composite of Hierarchical Pore Structure, *Small*. 13 (2017) 1601758, <https://doi.org/10.1002/smll.201601758>.
- M. Ghanbari, F. Soofivand, M. Salavati-Niasari, Simple synthesis and characterization of Ag₂Cd₄/AgI nanocomposite as an effective photocatalyst by co-precipitation method, *Journal of Molecular Liquids*. 223 (2016) 21–28, <https://doi.org/10.1016/j.molliq.2016.07.117>.
- M. Mousavi, A. Habibi-Yangjeh, S.R. Pouran, Review on magnetically separable graphitic carbon nitride-based nanocomposites as promising visible-light-driven photocatalysts, *Journal of Materials Science: Materials in Electronics*. 29 (2018) 1719–1747, <https://doi.org/10.1007/s10854-017-8166-x>.
- A. Akhundi, A. Habibi-Yangjeh, M. Abitorabi, S. Rahim Pouran, Review on photocatalytic conversion of carbon dioxide to value-added compounds and renewable fuels by graphitic carbon nitride-based photocatalysts, *Catalysis Reviews*. 61 (2019) 595–628, <https://doi.org/10.1080/01614940.2019.1654224>.
- D. Masih, Y. Ma, S. Rohani, Graphitic C₃N₄ based noble-metal-free photocatalyst systems: A review, *Applied Catalysis B: Environmental*. (2017) <https://doi.org/10.1016/j.apcatb.2017.01.061>.
- Y. Deng, L. Tang, G. Zeng, Z. Zhu, M. Yan, Y. Zhou, J. Wang, Y. Liu, J. Wang, Insight into highly efficient simultaneous photocatalytic removal of Cr(VI) and 2,4-dichlorophenol under visible light irradiation by phosphorus doped porous ultrathin g-C₃N₄ nanosheets from aqueous media: Performance and reaction mechanism, *Applied Catalysis B: Environmental*. 203 (2017) 343–354, <https://doi.org/10.1016/j.apcatb.2016.10.046>.
- Y. He, J. Cai, L. Zhang, X. Wang, H. Lin, B. Teng, L. Zhao, W. Weng, H. Wan, M. Fan, Comparing two new composite photocatalysts, t-LaVO₄/g-C₃N₄ and m-LaVO₄/g-C₃N₄, for their structures and performances, *Industrial and Engineering Chemistry Research*. 53 (2014) 5905–5915, <https://doi.org/10.1021/ie4043856>.
- L. Zhang, X. He, X. Xu, C. Liu, Y. Duan, L. Hou, Q. Zhou, C. Ma, X. Yang, R. Liu, F. Yang, L. Cui, C. Xu, Y. Li, Highly active TiO₂/g-C₃N₄/G photocatalyst with extended spectral response towards selective reduction of nitrobenzene, *Applied Catalysis B: Environmental*. 203 (2017) 1–8, <https://doi.org/10.1016/j.apcatb.2016.10.003>.
- J. Wang, Z. Guan, J. Huang, Q. Li, J. Yang, Enhanced photocatalytic mechanism for the hybrid g-C₃N₄/MoS₂ nanocomposite, *J. Mater. Chem. A* 2 (2014) 7960–7966, <https://doi.org/10.1039/C4TA00275J>.
- G. Tan, L. She, T. Liu, C. Xu, H. Ren, A. Xia, Ultrasonic chemical synthesis of hybrid mpg-C₃N₄/BiPO₄ heterostructured photocatalysts with improved visible light photocatalytic activity, *Applied Catalysis B: Environmental*. 207 (2017) 120–133, <https://doi.org/10.1016/j.apcatb.2017.02.025>.
- Z. Wan, G. Zhang, X. Wu, S. Yin, Novel visible-light-driven Z-scheme Bi₁₂GeO₂₀/g-C₃N₄ photocatalyst: Oxygen-induced pathway of organic pollutants degradation and proton assisted electron transfer mechanism of Cr(VI) reduction, *Applied Catalysis B: Environmental*. 207 (2017) 17–26, <https://doi.org/10.1016/j.apcatb.2017.02.014>.
- D. Jiang, T. Wang, Q. Xu, D. Li, S. Meng, M. Chen, Perovskite oxide ultrathin nanosheets/g-C₃N₄ 2D-2D heterojunction photocatalysts with significantly enhanced photocatalytic activity towards the photodegradation of tetracycline, *Applied Catalysis B: Environmental*. 201 (2017) 617–628, <https://doi.org/10.1016/j.apcatb.2016.09.001>.
- N. Zhang, C. Huang, P. Tong, Z. Feng, X. Wu, L. Zhang, Moisture stable Ni-Zn MOF/g-C₃N₄ nanoflowers: A highly efficient adsorbent for solid-phase microextraction of PAHs, *Journal of Chromatography A* 1556 (2018) 37–46, <https://doi.org/10.1016/j.chroma.2018.04.066>.
- J. Xu, J. Gao, Y. Qi, C. Wang, L. Wang, Anchoring Ni₂P on the UiO-66-NH₂/g-C₃N₄-derived C-doped ZrO₂/g-C₃N₄ Heterostructure: Highly Efficient Photocatalysts for H₂ Production from Water Splitting, *ChemCatChem*. 10 (2018) 3327–3335, <https://doi.org/10.1002/cctc.201800353>.

- [39] I.Y. Skobelev, A.B. Sorokin, K.A. Kovalenko, V.P. Fedin, O.A. Kholdeeva, Solvent-free allylic oxidation of alkenes with O₂ mediated by Fe- and Cr-MIL-101, *Journal of Catalysis*. 298 (2013) 61–69, <https://doi.org/10.1016/j.jcat.2012.11.003>.
- [40] X. Wang, F.M. Wisser, J. Canivet, M. Fontecave, C. Mellot-Draznieks, Immobilization of a Full Photosystem in the Large-Pore MIL-101 Metal-Organic Framework for CO₂ reduction, *ChemSusChem* 11 (2018) 3315–3322, <https://doi.org/10.1002/cssc.201801066>.
- [41] ECHA, MSC unanimously agrees that Bisphenol A is an endocrine disruptor, European Chemicals Agency: <https://echa.europa.eu/-/msc-unanimously-agrees-that-bisphenol-a-is-an-endocrine-disruptor>, 2017.
- [42] S. Ben Hammouda, F. Zhao, Z. Safaei, I. Babu, D.L. Ramasamy, M. Sillanpää, Reactivity of novel Ceria-Perovskite composites CeO₂-LaMO₃ (MCu, Fe) in the catalytic wet peroxidative oxidation of the new emergent pollutant “Bisphenol F”: Characterization, kinetic and mechanism studies, *Applied Catalysis B: Environmental*. 218 (2017) 119–136, <https://doi.org/10.1016/j.apcatb.2017.06.047>.
- [43] S. Ben Hammouda, F. Zhao, Z. Safaei, V. Srivastava, D. Lakshmi Ramasamy, S. Iftekhar, S. Kalliola, M. Sillanpää, Degradation and mineralization of phenol in aqueous medium by heterogeneous monopersulfate activation on nanostructured cobalt based-perovskite catalysts ACoO₃ (A = La, Ba, Sr and Ce): Characterization, kinetics and mechanism study, *Applied Catalysis B: Environmental*. 215 (2017) 60–73, <https://doi.org/10.1016/j.apcatb.2017.05.051>.
- [44] S. Ben Hammouda, F. Zhao, Z. Safaei, D.L. Ramasamy, B. Doshi, M. Sillanpää, Sulfate radical-mediated degradation and mineralization of bisphenol F in neutral medium by the novel magnetic Sr₂CoFeO₆ double perovskite oxide catalyzed peroxymonosulfate: Influence of co-existing chemicals and UV irradiation, *Applied Catalysis B: Environmental*. 233 (2018) 99–111, <https://doi.org/10.1016/j.apcatb.2018.03.088>.
- [45] H. Li, J. Liu, W. Hou, N. Du, R. Zhang, X. Tao, Synthesis and characterization of g-C₃N₄/Bi₂MoO₆ heterojunctions with enhanced visible light photocatalytic activity, *Applied Catalysis B: Environmental* 160–161 (2014) 89–97, <https://doi.org/10.1016/j.apcatb.2014.05.019>.
- [46] Y. Fu, T. Huang, L. Zhang, J. Zhu, X. Wang, Ag/g-C₃N₄ catalyst with superior catalytic performance for the degradation of dyes: a borohydride-generated superoxide radical approach, *Nanoscale* 7 (2015) 13723–13733, <https://doi.org/10.1039/c5nr03260a>.
- [47] A. Idris, N. Hassan, R. Rashid, A.-F. Ngomsik, Kinetic and regeneration studies of photocatalytic magnetic separable beads for chromium (VI) reduction under sunlight, *Journal of Hazardous Materials*. 186 (2011) 629–635, <https://doi.org/10.1016/j.jhazmat.2010.11.101>.
- [48] F. Cui, Q. Deng, L. Sun, Prussian blue modified metal-organic framework MIL-101(Fe) with intrinsic peroxidase-like catalytic activity as a colorimetric biosensing platform, *RSC Advances*. 5 (2015) 98215–98221, <https://doi.org/10.1039/C5RA18589K>.
- [49] C. Yang, X. You, J. Cheng, H. Zheng, Y. Chen, A novel visible-light-driven In-based MOF/graphene oxide composite photocatalyst with enhanced photocatalytic activity toward the degradation of amoxicillin, *Applied Catalysis B: Environmental*. 200 (2017) 673–680, <https://doi.org/10.1016/j.apcatb.2016.07.057>.
- [50] A. Abbasi, D. Ghanbari, M. Salavati-Niasari, M. Hamadani, Photo-degradation of methylene blue: photocatalyst and magnetic investigation of Fe₂O₃-TiO₂ nanoparticles and nanocomposites, *Journal of Materials Science: Materials in Electronics* 27 (2016) 4800–4809, <https://doi.org/10.1007/s10854-016-4361-4>.
- [51] W. Huang, N. Liu, X. Zhang, M. Wu, L. Tang, Metal organic framework g-C₃N₄/MIL-53(Fe) heterojunctions with enhanced photocatalytic activity for Cr(VI) reduction under visible light, *Applied Surface Science* 425 (2017) 107–116, <https://doi.org/10.1016/j.apsusc.2017.07.050>.
- [52] H. Wang, X. Yuan, Y. Wu, G. Zeng, X. Chen, L. Leng, H. Li, Synthesis and applications of novel graphitic carbon nitride/metal-organic frameworks mesoporous photocatalyst for dyes removal, *Applied Catalysis B: Environmental*. 174–175 (2015) 445–454, <https://doi.org/10.1016/j.apcatb.2015.03.037>.
- [53] H. Shi, G. Chen, C. Zhang, Z. Zou, Polymeric g-C₃N₄ Coupled with NaNbO₃ Nanowires toward Enhanced Photocatalytic Reduction of CO₂ into Renewable Fuel, *ACS Catalysis* 4 (2014) 3637–3643, <https://doi.org/10.1021/cs500848f>.
- [54] S. Ye, L.-G. Qiu, Y.-P. Yuan, Y.-J. Zhu, J. Xia, J.-F. Zhu, Facile fabrication of magnetically separable graphitic carbon nitride photocatalysts with enhanced photocatalytic activity under visible light, *Journal of Materials Chemistry A*. 1 (2013) 3008, <https://doi.org/10.1039/c2ta01069k>.
- [55] X. Zhu, N. Guijarro, Y. Liu, P. Schouwink, R.A. Wells, F. Le Formal, S. Sun, C. Gao, K. Sivula, Spinel Structural Disorder Influences Solar-Water-Splitting Performance of ZnFe₂O₄ Nanorod Photoanodes, *Advanced Materials*. 30 (2018) 1801612, <https://doi.org/10.1002/adma.201801612>.
- [56] Y. Liu, F. Le Formal, F. Boudoire, N. Guijarro, Hematite Photoanodes for Solar Water Splitting: A Detailed Spectroelectrochemical Analysis on the pH-Dependent Performance, *ACS Applied Energy Materials*. 2 (2019) 6825–6833, <https://doi.org/10.1021/acsaem.9b01261>.
- [57] Y. Zuo, Y. Liu, J. Li, R. Du, X. Yu, C. Xing, T. Zhang, L. Yao, J. Arbiol, J. Llorca, K. Sivula, N. Guijarro, A. Cabot, Solution-Processed Ultrathin SnS 2–Pt Nanoplates for Photoelectrochemical Water Oxidation, *ACS Applied Materials & Interfaces*. 11 (2019) 6918–6926, <https://doi.org/10.1021/acsaami.8b17622>.
- [58] Y. Liu, F. Le Formal, F. Boudoire, L. Yao, K. Sivula, N. Guijarro, Insights into the interfacial carrier behaviour of copper ferrite (CuFe₂O₄) photoanodes for solar water oxidation, *Journal of Materials Chemistry A7* (2019) 1669–1677, <https://doi.org/10.1039/C8TA11160J>.
- [59] Y. Bu, Z. Chen, W. Li, Using electrochemical methods to study the promotion mechanism of the photoelectric conversion performance of Ag-modified mesoporous g-C₃N₄ heterojunction material, *Applied Catalysis B: Environmental*. 144 (2014) 622–630, <https://doi.org/10.1016/j.apcatb.2013.07.066>.
- [60] H. Fu, G. Lu, S. Li, Adsorption of Chromium(VI) Ions on to TiO₂ from Aqueous Solution, *Adsorption Science & Technology*. 16 (1998) 117–126, <https://doi.org/10.1177/026361749801600205>.
- [61] F. Zhao, Z. Yang, Z. Wei, R. Spinney, M. Sillanpää, J. Tang, M. Tam, R. Xiao, Polyethylenimine-modified chitosan materials for the recovery of La (III) from leachates of bauxite residue, *Chemical Engineering Journal*. 388 (2020) 124307, <https://doi.org/10.1016/j.cej.2020.124307>.
- [62] F. Zhao, E. Repo, D. Yin, M.E.T. Sillanpää, Adsorption of Cd(II) and Pb(II) by a novel EGTA-modified chitosan material: Kinetics and isotherms, *Journal of Colloid and Interface Science*. 409 (2013) 174–182.
- [63] C.C. Wang, X.D. Du, J. Li, X.X. Guo, P. Wang, J. Zhang, Photocatalytic Cr(VI) reduction in metal-organic frameworks: A mini-review, *Applied Catalysis B: Environmental*. 193 (2016) 198–216, <https://doi.org/10.1016/j.apcatb.2016.04.030>.
- [64] Q. Jiang, A.-M. Spehar, M. Håkansson, J. Suomi, T. Ala-Kleme, S. Kulmala, Hot electron-induced cathodic electrochemiluminescence of rhodamine B at disposable oxide-coated aluminum electrodes, *Electrochimica Acta*. 51 (2006) 2706–2714, <https://doi.org/10.1016/j.electacta.2005.08.004>.
- [65] F. Liu, W. Zhang, L. Tao, B. Hao, J. Zhang, Simultaneous photocatalytic redox removal of chromium(VI) and arsenic(III) by hydrothermal carbon-sphere@nano-Fe₃O₄, *Environmental Science: Nano*. 6 (2019) 937–947, <https://doi.org/10.1039/C8EN01362D>.
- [66] S. Chen, Y. Hu, S. Meng, X. Fu, Study on the separation mechanisms of photogenerated electrons and holes for composite photocatalysts g-C₃N₄-WO₃, *Applied Catalysis B: Environmental*. 150–151 (2014) 564–573, <https://doi.org/10.1016/j.apcatb.2013.12.053>.
- [67] W. Liu, Y. Li, F. Liu, W. Jiang, D. Zhang, J. Liang, Visible-light-driven photocatalytic degradation of diclofenac by carbon quantum dots modified porous g-C₃N₄: Mechanisms, degradation pathway and DFT calculation, *Water Research*. 151 (2019) 8–19, <https://doi.org/10.1016/j.watres.2018.11.084>.
- [68] X. Liang, G. Wang, X. Dong, G. Wang, H. Ma, X. Zhang, Graphitic Carbon Nitride with Carbon Vacancies for Photocatalytic Degradation of Bisphenol A, *ACS Applied Nano Materials*. 2 (2019) 517–524, <https://doi.org/10.1021/acsnano.8b02089>.
- [69] R. Xiao, L. He, Z. Luo, R. Spinney, Z. Wei, D.D. Dionysiou, F. Zhao, An experimental and theoretical study on the degradation of clonidine by hydroxyl and sulfate radicals, *Science of The Total Environment*. 710 (2020) 136333, <https://doi.org/10.1016/j.scitotenv.2019.136333>.
- [70] D. Huang, Z. Li, G. Zeng, C. Zhou, W. Xue, X. Gong, X. Yan, S. Chen, W. Wang, M. Cheng, Megamerger in photocatalytic field: 2D g-C₃N₄ nanosheets serve as support of 0D nanomaterials for improving photocatalytic performance, *Applied Catalysis B: Environmental*. 240 (2019) 153–173, <https://doi.org/10.1016/j.apcatb.2018.08.071>.
- [71] Q. Xu, L. Zhang, J. Yu, S. Wageh, A.A. Al-Ghamdi, M. Jaroniec, Direct Z-scheme photocatalysts: Principles, synthesis, and applications, *Materials Today* 21 (2018) 1042–1063, <https://doi.org/10.1016/j.mat.2018.04.008>.
- [72] J. Jiang, X. Yuan, Y. Pan, J. Liang, G. Zeng, Z. Wu, H. Wang, Doping of graphitic carbon nitride for photocatalysis: A review, *Applied Catalysis B: Environmental*. 217 (2017) 388–406, <https://doi.org/10.1016/j.apcatb.2017.06.003>.
- [73] W. Zhang, G. Li, W. Wang, Y. Qin, T. An, X. Xiao, W. Choi, Enhanced photocatalytic mechanism of Ag₃PO₄ nano-sheets using MS₂ (M = Mo, W)/rGO hybrids as co-catalysts for 4-nitrophenol degradation in water, *Applied Catalysis B: Environmental*. 232 (2018) 11–18, <https://doi.org/10.1016/j.apcatb.2018.03.006>.
- [74] J. Fu, Q. Xu, J. Low, C. Jiang, J. Yu, Ultrathin 2D/2D WO₃/g-C₃N₄ step-scheme H₂-production photocatalyst, *Applied Catalysis B: Environmental*. 243 (2019) 556–565, <https://doi.org/10.1016/j.apcatb.2018.11.011>.
- [75] L. Shi, Y. Yin, L.-C. Zhang, S. Wang, M. Sillanpää, H. Sun, Design and engineering heterojunctions for the photoelectrochemical monitoring of environmental pollutants: A review, *Applied Catalysis B: Environmental*. 248 (2019) 405–422, <https://doi.org/10.1016/j.apcatb.2019.02.044>.
- [76] D. Xia, W. Wang, R. Yin, Z. Jiang, T. An, G. Li, H. Zhao, P.K. Wong, Enhanced photocatalytic inactivation of *Escherichia coli* by a novel Z-scheme g-C₃N₄/m-Bi₂O₃ hybrid photocatalyst under visible light: The role of reactive oxygen species, *Applied Catalysis B: Environmental*. 214 (2017) 23–33, <https://doi.org/10.1016/j.apcatb.2017.05.035>.
- [77] H. Gao, R. Cao, X. Xu, S. Zhang, H. Yongshun, H. Yang, X. Deng, J. Li, Construction of dual defect mediated Z-scheme photocatalysts for enhanced photocatalytic hydrogen evolution, *Applied Catalysis B: Environmental*. 245 (2019) 399–409, <https://doi.org/10.1016/j.apcatb.2019.01.004>.
- [78] D. Masih, Y. Ma, S. Rohani, Graphitic C₃N₄ based noble-metal-free photocatalyst systems: A review, *Applied Catalysis B: Environmental*. 206 (2017) 556–588, <https://doi.org/10.1016/j.apcatb.2017.01.061>.
- [79] A.K. Sarkar, A. Saha, A. Tarafder, A.B. Panda, S. Pal, Efficient Removal of Toxic Dyes via Simultaneous Adsorption and Solar Light Driven Photodegradation Using Recyclable Functionalized Amylopectin-TiO₂-Au Nanocomposite, *ACS Sustainable Chemistry & Engineering*. 4 (2016) 1679–1688, <https://doi.org/10.1021/acscuschemeng.5b01614>.
- [80] C. Xing, Y. Liu, Y. Zhang, J. Liu, T. Zhang, P. Tang, J. Arbiol, L. Soler, K. Sivula, N. Guijarro, X. Wang, J. Li, R. Du, Y. Zuo, A. Cabot, J. Llorca, Porous NiTiO₃/TiO₂ nanostructures for photocatalytic hydrogen evolution, *Journal of Materials Chemistry A*. 7 (2019) 17053–17059, <https://doi.org/10.1039/C9TA04763H>.